Title	Prograde infiltration of Cl-rich fluid into the granulitic continental crust from a collision zone in East Antarctica (Perlebandet, Sør Rondane Mountains)
Author(s)	Kawakami, Tetsuo; Higashino, Fumiko; Skrzypek, Etienne; Satish-Kumar, M.; Grantham, Geoffrey; Tsuchiya, Noriyoshi; Ishikawa, Masahiro; Sakata, Shuhei; Hirata, Takafumi
Citation	Lithos (2017), 274-275: 73-92
Issue Date	2017-03
URL	http://hdl.handle.net/2433/229508
Right	© 2017. This manuscript version is made available under the CC-BY-NC-ND 4.0 license http://creativecommons.org/licenses/by-nc-nd/4.0/; The full-text file will be made open to the public on 01 March 2019 in accordance with publisher's 'Terms and Conditions for Self-Archiving'; This is not the published version. Please cite only the published version. この論文は出版社版でありません。引用の際には出版社版をご確認ご利用ください。
Type	Journal Article
Textversion	author

Prograde infiltration of Cl-rich fluid into the granulitic continental crust from a collision zone in East Antarctica (Perlebandet, Sør Rondane Mountains)

Tetsuo Kawakami[1,*], Fumiko Higashino[1,2], Etienne Skrzypek[1], M. Satish-Kumar[3], Geoffrey Grantham[4], Noriyoshi Tsuchiya[5], Masahiro Ishikawa[6], Shuhei Sakata[1], Takafumi Hirata[1]

1 Department of Geology and Mineralogy, Graduate School of Science, Kyoto University, Kitashirakawa-Oiwake-cho, Sakyo-ku, Kyoto 606-8502, Japan

2 Research Fellow of Japan Society for the Promotion of Science

3 Department of Geology, Faculty of Science, Niigata University, 2-8050 Ikarashi, Nishi-ku, Niigata 950-2181, Japan

4 Department of Geology, University of Johannesburg, PO Box 524, Auckland Park, 2006, South Africa

5 Department of Geoscience and Technology, Graduate School of Engineering, Tohoku University, Aramaki, Aoba-ku, Sendai 980-9570, Japan

6 Graduate School of Environment and Information Sciences, Yokohama National University, Tokiwadai, Hodogaya-ku, Yokohama 240-8501, Japan

*Corresponding author; t-kawakami@kueps.kyoto-u.ac.jp

Abstract

Utilizing microstructures of Cl-bearing biotite in pelitic and felsic metamorphic rocks, the timing of Cl-rich fluid infiltration is correlated with the pressure-temperature-time (*P-T-t*) path of upper amphibolite- to granulite-facies metamorphic rocks from Perlebandet, Sør Rondane Mountains (SRM), East Antarctica. Microstructural observation indicates that the stable Al_2SiO_5 polymorph changed from sillimanite to kyanite + andalusite + sillimanite, and *P-T* estimates from geothermobarometry point to a counterclockwise *P-T* path characteristic of the SW terrane of the SRM. *In situ* laser ablation inductively coupled plasma mass spectrometry for U-Pb dating of zircon inclusions in garnet yielded ca. 580 Ma, likely representing the age of garnet-forming metamorphism at Perlebandet.

Inclusion-host relationships among garnet, sillimanite, and Cl-rich biotite (Cl > 0.4 wt%) reveal that formation of Cl-rich biotite took place during prograde metamorphism in the sillimanite stability field. This process probably predated partial melting consuming biotite (Cl = 0.1-0.3 wt%). This was followed by retrograde, moderately Cl-bearing biotite (Cl = 0.1-0.3 wt%) replacing garnet. Similar

timings of Cl-rich biotite formation in different samples, and similar $f(H_2O)/f(HCl)$ values of coexisting fluid estimated for each stage can be best explained by prograde Cl-rich fluid infiltration. Fluid-present partial melting at the onset of prograde metamorphism probably contributed to elevate the Cl concentration (and possibly salinity) of the fluid, and consumption of the fluid resulted in the progress of dehydration melting. The retrograde fluid was released from crystallizing Cl-bearing partial melts or derived externally. The prograde Cl-rich fluid infiltration in Perlebandet presumably took place at the uppermost part of the footwall of the collision boundary. Localized distribution of Cl-rich biotite and hornblende along large-scale shear zones and detachments in the SRM supports external input of Cl-rich fluids through tectonic boundaries during continental collision.

Keywords: fluid, brine, partial melting, Al_2SiO_5 polymorphs, chlorine, continental collision

Introduction

Low water activity fluids have been recognized as the major fluid species present under granulite facies conditions prevailing in the lower continental crust (Aranovich et al., 1987; Newton et al., 1998; Touret and Huizenga, 2011). Under such conditions, brines can immiscibly coexist with CO_2-rich fluids (Heinrich, 2007). Direct evidence of highly saline brine, such as fluid inclusions (van den Berg and Huizenga, 2001) and/or salt crystals (e.g., Markl and Bucher, 1998) have been reported, although they are relatively uncommon. Rare preservation of brines as fluid inclusions is attributed to the low viscosity and low wetting angle of brines (Watson and Brenan, 1987; Holness, 1997) that make it easy for brine to escape the rock. In addition, steep isochores of NaCl-H_2O fluids in pressure-temperature (*P*-*T*) space result in gross overpressurization of brine inclusions during heating and decrepitation or implosion during isobaric cooling (Touret et al., 2016). These features probably hindered understanding of the timing and spatial distribution of brines in high-grade metamorphic terranes.

The presence of Cl-rich biotite, hornblende and apatite is often taken as evidence for the presence of Cl-bearing fluids and brines (e.g., Harlov and Förster, 2002; Higashino et al., 2013a; Safonov et al., 2014). These minerals are known to incorporate Cl in place of OH in their crystal structures when they exchange with Cl-bearing fluids (e.g., Munoz and Swenson, 1981; Kullerud, 1996). Data on Cl partitioning between fluids and these minerals is available (e.g., Zhu and Sverjensky, 1991; 1992; Mathez and Webster, 2005); the $f(H_2O)/f(HCl)$ ratio of the coexisting fluid can be estimated from the composition of biotite and apatite (e.g., Selby and Nesbitt, 2000). In partially molten, migmatitic pelitic gneisses, Cl-rich biotite may coexist with nanogranite/felsite inclusions (Kawakami et al., 2016; see Hiroi et al. (2014) for 'felsite inclusions'), and thus not only subsolidus Cl-rich aqueous fluid infiltration but also processes involving partial melting can lead to the formation of Cl-rich biotite.

This study aims to correlate the reconstructed *P*-*T*-*t* path with partial melting and Cl-rich fluid infiltration events using microstructural observations pointing to several stages of Cl-bearing biotite formation in pelitic and felsic gneisses from Perlebandet (western Sør Rondane Mountains (SRM), East Antarctica). We discuss multiple Cl-bearing fluid infiltration events in the SRM. Mineral abbreviations are after Kretz (1983).

Geological setting

The Sør Rondane Mountains

In the SRM (22º-28ºE, 71.5º-72.5ºS) of eastern Dronning Maud Land, East Antarctica (Fig. 1a), the granulite facies lower continental crust of a continental collision setting is widely exposed (Shiraishi et al., 1991; Asami et al., 1992). The SRM are thought to be a part of the collision zone between East and West Gondwana during the ca. 750–620 Ma 'East African-Antarctic Orogeny (EAAO)' (Jacobs et al., 2003) and are also affected by the ca. 570–500 Ma 'Kuunga Orogeny' (Meert, 2003). Apparent depositional ages of metacarbonate rocks from Balchenfjella, Brattnipene, Menipa and Tanngarden regions in the SRM (Fig. 1b) are estimated as late-Tonian and early-Cryogenian age (880–850 Ma and 820–790 Ma) based on a Sr isotope study (Otsuji et al., 2013). Protoliths of metacarbonates are considered to have been deposited in the Mozambique Ocean that separated the continental blocks that amalgamated to form Gondwana (Otsuji et al., 2013).

The SRM is divided into the NE and SW terranes which are separated by a gently N- to

NE-dipping mylonite zone named the Main Tectonic Boundary (MTB; Osanai et al., 2013) (Fig. 1b). The NE terrane is mainly composed of amphibolite- to granulite-facies metamorphic rocks of pelitic, psammitic, and intermediate compositions (Shiraishi and Kojima, 1987; Asami and Shiraishi, 1987; Grew et al., 1989) showing clockwise *P-T* paths (Osanai et al., 2013; Grantham et al., 2013). In contrast, the SW terrane is composed of granulite- to greenschist-facies rocks with a large volume of meta-tonalite (Fig. 1b; Shiraishi et al., 2008; Kamei et al., 2013), showing counterclockwise *P-T* paths (Adachi et al., 2013; Baba et al., 2013). U-Pb ages of detrital zircon are also different between these two terranes; detrital zircons older than 1200 Ma are absent from the SW terrane (Osanai et al., 2013; Kitano et al., 2016). Based on these observations, the two different *P-T* paths in these adjoining terranes are explained by the collision between these two terranes, with the NE-terrane thrusted over the SW-terrane during the EAAO at 650-600 Ma, followed by amphibolite-facies metamorphism at ca. 570 Ma (Osanai et al., 2013). A SE-dipping ductile extensional shear zone termed the Balchen Detachment Fault (BDF) structurally divides Balchenfjella (Fig. 1b), and the southeastward movement of the Berrheia unit (hanging wall side) with respect to the Gropeheia unit (footwall side) is inferred to represent an extensional deformation phase between ca. 600 Ma and ca. 549 Ma (Ishikawa et al., 2013), which is interpreted to result from extensional collapse after crustal overthickening.

The Main Shear Zone (Kojima and Shiraishi, 1986; Fig. 1b) that defines the boundary between older meta-tonalite and amphibolite-facies metamorphic rocks in the SW-terrane was inferred to have limited tectonic significance by Osanai et al. (2013). However, Ruppel et al. (2015) interpreted it to be a large-scale late Pan-African strike-slip structure of ca. 560-530 Ma, representing an important lithotectonic boundary separating East African affinities from 'Indo-Antarctic' Rayner-age affinities presumably close to the eastern margin of the EAAO (Ruppel et al., 2015).

The SRM is also interpreted to be a part of the hanging wall of a mega-nappe complex which formed through continental collision between northern and southern Gondwana during the Kuunga Orogeny at 580–540 Ma (Grantham et al., 2008; 2013), as supported by the data from part of the NE terrane (Balchenfjella and Austhameren; Fig. 1b).

In the SRM, Cl-rich biotite, apatite and hornblende have been described in felsic and mafic gneisses along the large scale shear zones and tectonic boundaries which extend over 200 km (Higashino et al., 2013a; 2013b; 2015a; Fig. 1b). In eastern SRM (Balchenfjella; Fig. 1b), Cl-rich biotite and apatite in pelitic gneisses have been interpreted to have resulted from interaction with a Cl-rich fluid or melt that was present at near peak metamorphic condition of ca. 0.8 GPa and 800 °C (Higashino et al., 2013a). In the central SRM (Brattnipene; Fig. 1b), Cl-rich hornblende and biotite are formed along garnet-hornblende veins, and 'diffusion-like' profiles of Cl content in hornblende and biotite decreasing from the vein towards the wall rock are observed (Higashino et al., 2015b). Mass balance analysis revealed that elements mobile in brines rather than in melts were added to the wall rock, suggesting that brine infiltration produced the garnet-hornblende veins in Brattnipene

(Higashino et al., 2015b).

In addition to these Cl-rich minerals in metamorphic rocks, magmatic hornblende and biotite show relatively high Cl contents in some granitoids in the SRM. Li et al. (2003, 2007) reported 0.28-0.32 wt.% Cl in hornblende from the Dufek granite, and 0.31-0.41 wt.% Cl in hornblende and 0.21-0.59 wt.% Cl in biotite from the Pingvinane granite (Fig. 1b). The U-Pb zircon age determined by SHRIMP or laser ablation inductively coupled plasma mass spectrometry (LA-ICPMS) is 619 ± 7 Ma (Li et al., 2006) and 637 ± 6 Ma (Elburg et al., 2016) for the Dufek granite, and 506 ± 4 Ma (Elburg et al., 2016) for the Pingvinane granite.

Perlebandet

Perlebandet is one of the westernmost nunataks in the SRM, where granulite facies layered gneisses are exposed (Fig. 1c). It is a key area to constrain the location of the MTB, and has been considered to belong to the NE terrane (Osanai et al., 2013) in the lack of detailed information of *P-T* path of this area. However, Perlebandet is interpreted to be part of the SW terrane on the basis of magnetic surveys (Mieth et al., 2014).

The main lithologies observed in Perlebandet are garnet-biotite (Grt-Bt) gneiss, garnet-sillimanite-biotite (Grt-Sil-Bt) gneiss, hornblende-biotite gneiss, marble and skarns, pyroxene granulite, and orthopyroxene-bearing amphibolite (Fig. 1c; Shiraishi et al., 1997). Previous SHRIMP

U-Pb zircon dating of a Sil-Grt-Bt gneiss from Perlebandet gave an inherited core age of 1009 ± 13 Ma, and rim ages of 736 ± 13 Ma, 609 ± 11 Ma, and 565 ± 7 Ma (Shiraishi et al., 2008). Among the three rim ages, the latter two are considered as metamorphic, whereas the detrital or metamorphic origin of the first one remains unclear (Shiraishi et al., 2008). Sillimanite is the most common aluminosilicate mineral, and retrograde andalusite and kyanite are locally present (Kawakami et al., 2010). Otsuji et al. (2013) reported low Sr and oxygen isotope ratios from Perlebandet metacarbonates, which are not characteristic of continental settings. These low Sr isotope ratios can be attributed to interaction with low Sr-bearing magmatic fluids or to the older depositional age of Perlebandet metacarbonates compared to that from other parts of the SRM (Otsuji et al., 2013). Otsuji et al. (2016) further pointed out that Nd and Sr isotopic data from metacarbonate rocks from Perlebandet neither match the data from the rocks in the SW terrane, nor from the Balchenfjella in the NE terrane. Based on these data, they proposed that Perlebandet carbonates were deposited in an environment surrounding an isolated seamount in the Tonian to Cryogenian period, and that amalgamation of Gondwana and the final closure of Mozambique Ocean and East Antarctic Ocean took place at ca. 660-550 Ma (Otsuji et al., 2016).

Analytical methods

Quantitative analysis of rock-forming minerals and X-ray elemental mapping of thin section samples were performed by a JEOL JXA-8105 superprobe. Analytical conditions for quantitative analyses except for apatite were 15.0 kV acceleration voltage, 10 nA beam current, and 3 μm beam diameter. The counting time for the peak and backgrounds was 30 s and 15 s for Cl, 60 s and 30 s for F, and 10 s and 5 s for other elements. Analytical conditions for quantitative analysis of apatite followed that recommended by Goldoff et al (2012). Natural and synthetic minerals (Astimex MINM25-53) were used as standards and ZAF correction was applied. Analytical conditions for X-ray elemental mappings were acceleration voltage of 15.0 kV, probe current of 50 nA, focused beam to 3 μm beam diameter, and dwell time of 25-40 milliseconds. Electron microprobe analysis of rutile was also done by a JEOL JXA-8105 superprobe, following analytical conditions recommended by Zack et al. (2004).

Cathodoluminescence (CL) images were obtained using a JEOL JXA-8105 superprobe equipped with Hamamatsu Photonics high voltage power supply C9525 and photon counting unit C9744. Analytical conditions for CL mapping were 15.0 kV acceleration voltage, 1 nA beam current, focused beam to 10 μm beam diameter, and dwell time of 1 msec.

Minerals were also qualitatively identified by a Hitachi S3500H scanning electron microscope equipped with an EDAX X-ray analytical system. Laser Raman spectroscopy (JASCO NRS 3100) was used to identify Al_2SiO_5 minerals.

In situ zircon U-Pb dating on thin section samples via LA-ICP-MS was carried out using a Nu Plasma II HR-MC-ICPMS coupled to a NWR femtosecond laser-ablation system. Backscattered electron (BSE) and CL images were obtained prior to the analyses to identify spot positions, overlapping multiple growth zones, grain edges, cracks or damaged zircon grains. Detailed analytical conditions of the LA-ICP-MS analysis are given in Higashino et al. (2015a). Data were processed and plotted using *Isoplot 4.15* (Ludwig, 2012). All of the above analyses were done at the Department of Geology and Mineralogy, Graduate School of Science, Kyoto University.

Sample localities and sample descriptions

The samples used in this study are two Grt-Bt gneisses [samplesTK2009113001B (3001B) and TK2009112601C (2601C)] and three Grt-Sil-Bt gneisses [samples TK2009113001G (3001G), TK2009113001H (3001H) and TK2009112602D (2602D)] collected during the summer season of the 51st Japan Antarctic Research Expedition (JARE51; Tsuchiya et al., 2012). Samples were collected from the northern half of Perlebandet (Fig. 1c). The common Al_2SiO_5 mineral in these gneisses is sillimanite, found as inclusions in cores of garnet and as a matrix mineral defining the gneissose structure (Fig. 2a-d). A rare sample with strong retrogression (sample 3001G) contains secondary andalusite, kyanite, and sillimanite replacing garnet (Fig. 2e-n). Detailed descriptions of the samples studied are given below, and representative mineral analyses are given in Table 1.

Garnet-sillimanite-biotite gneiss (samples 2602D and 3001H)

These gneisses consist of garnet, sillimanite, biotite, K-feldspar, quartz and plagioclase (An19-23 in 2602D, and An13-17 in 3001H), and subordinate rutile, ilmenite, zircon, monazite and apatite. Muscovite is only present as a secondary mineral. Sillimanite is abundant in the matrix and also present as inclusions in cores of garnet (X_{Mg} = 0.25-0.29 in 2602D, and X_{Mg} = 0.25-0.32 in 3001H) (Fig. 2a). Biotite is not included in garnet. Garnet is replaced by secondary biotite at the rim and along the cracks. It does not preserve chemical zoning, except for the rims and along the cracks affected by the retrograde re-equilibration. The highest X_{Mg} content of garnet is preserved distant from the cracks where the retrograde effects are minimal. In both samples, sillimanite and biotite partly replace garnet rim. Retrograde biotite tends to have lower TiO_2 contents compared to matrix biotite. Cracks in garnet are filled with retrograde biotite with the lowest Cl (Cl ~ 0.01 wt.%) and the lowest TiO_2 (< 0.29 wt.%) contents.

In sample 2602D, garnet rim contain inclusions of quartz and K-feldspar. Matrix biotite has moderate Cl content (0.17-0.22 wt.%, X_{Mg} = 0.41-0.51) and the highest TiO_2 content (2.04-3.96 wt.%). Retrograde biotite (Cl < 0.15 wt.%, TiO_2 = 0.98-2.82 wt.%, X_{Mg} = 0.45-0.48) and plagioclase (An18-23) replace garnet at the rim (X_{Mg} = 0.11-0.13). Matrix sillimanite very rarely includes garnet (X_{Mg} = 0.23-0.24). Rutile in the matrix and that included in sillimanite gave Zr contents of 1125-1466 ppm (average = 1359 ppm; 8 points) and 1917-1947 ppm, respectively.

In sample 3001H, some sillimanite grains contain inclusions of green spinel. Biotite in this sample has very low Cl content (Cl < 0.03 wt.%, X_{Mg} = 0.42-0.49) irrespective of its mode of occurrence. Garnet is replaced by biotite (Cl < 0.02 wt.%) and plagioclase (An16-18) at the rim (X_{Mg} = 0.10-0.12). Matrix sillimanite rarely includes rutile (Zr = 1473-1636 ppm). Rutile in the matrix has a Zr content of 1125-2162 ppm (average = 1712 ppm; 15 points).

Strongly retrogressed garnet-sillimanite-biotite gneiss (sample 3001G)

This is a folded, pelitic gneiss with sillimanite porphyroblasts (ca. 1cm in length). The matrix of this gneiss mainly consists of biotite, garnet, sillimanite, K-feldspar, plagioclase (An26-31), quartz and retrograde andalusite, kyanite, sillimanite and muscovite (Fig. 2b-n). K-feldspar is especially abundant in the matrix (Fig. 2e-f). Accessory minerals are ilmenite, zircon, monazite and rare rutile. Ti-oxide minerals are mostly ilmenite in the matrix, but rare rutile (Zr = 874-1273 ppm; average of 15 points = 1139 ppm) is preserved as inclusions in garnet (Fig. 2o) and in K-feldspar. Myrmekite is also present in the matrix. Garnet in this sample is strongly replaced mainly by biotite, plagioclase, andalusite, kyanite, and sillimanite (Fig. 2e-n).

Sillimanite is the only Al_2SiO_5 mineral included in garnet. Prismatic sillimanite porphyroblast in the matrix has an inclusion-poor core and inclusion-rich rim (Fig. 2b, c). Sillimanite porphyroblasts up to 1 cm in diameter show numerous subgrains and often includes smaller prismatic sillimanite with crystallographic orientations different from that of the host sillimanite (Fig. 2c). The core of sillimanite porphyroblast includes plagioclase (An33-37), K-feldspar and moderately Cl-bearing biotite (0.17-0.30 wt.%; Table 1). The rim of sillimanite can be recognized by the presence of abundant inclusions of Zn-bearing spinel (ZnO = 4-6 wt.%, X_{Mg} [= Mg/(Mg+Fe_{total})] = 0.18-0.22), plagioclase (An31-35), garnet (X_{Mg} = 0.18-0.19), biotite (Cl < 0.32 wt.%), ilmenite, and rare quartz (Fig. 2c, d). Sillimanite that is replacing garnet (Fig. 2e, i, j) commonly includes Zn-bearing spinel crystals, resembling the rim of prismatic sillimanite in the matrix. Randomly-oriented, fibrolitic sillimanite is locally formed along the grain boundaries of matrix minerals.

Garnet is mostly xenomorphic, and includes sillimanite, Zn-bearing spinel, biotite, plagioclase, quartz, ilmenite and zircon (Fig. 2k-n). It is replaced by retrograde minerals such as biotite, andalusite, kyanite, sillimanite, muscovite, plagioclase and quartz (Fig. 2f-n). Replacement by biotite + plagioclase intergrowths is also common (Fig. 2i-j). Garnet that locally includes Zn-bearing spinel overgrows sillimanite porphyroblasts (Fig. 2b-d). Spinel included in such garnet is more Zn-rich than that included in sillimanite. Garnet that overgrows sillimanite and separate garnet grains in the matrix both show decreasing X_{Mg} from the core (X_{Mg} = 0.15-0.21) to the rim (X_{Mg} = 0.10-0.14). The X_{Ca} [= Ca/(Fe+Mn+Mg+Ca)] slightly decreases towards the rim or remains constant at 0.04-0.07 (Table 1). These garnet zonings are diffuse and are strongly affected by retrograde re-equilibration.

Biotite included in garnet-overgrowth on sillimanite (Fig. 2b) shows high Cl (< 0.41wt.% Cl) and X_{Mg} (~ 0.63) and varying TiO_2 (2.3-6.0 wt.%) (Fig. 3a, b). Biotite included in sillimanite porphyroblast shows moderate Cl contents (0.17-0.30 wt.%) with high X_{Mg} (0.46-0.56) and varying TiO_2 (2.8-5.0 wt.%) (Fig. 3a, b). Matrix biotite shows moderate Cl contents (0.13-0.25 wt.%) with lower X_{Mg} (~ 0.40) and moderate TiO_2 (2.5-3.6 wt.%) (Fig. 3a, b). Biotite in the biotite-plagioclase intergrowth replacing garnet (Fig. 2g, i) shows moderate TiO_2 (3.2-4.2 wt.%) and Cl (0.17-0.24 wt.%) contents and X_{Mg} (~ 0.47) value (Fig. 3a, b). Apparently retrograde, crack-filling biotite in garnet (Fig. 2k-n) shows moderate to low Cl (0.09-0.16 wt.%) and low TiO_2 (1.9-2.5 wt.%) contents (Fig. 3a, b). Retrograde biotite developed at garnet rims also shows similar compositions to the crack-filling biotite (Fig. 3a, b). There is a clear tendency for prograde biotites, such as inclusions in garnet and sillimanite and some of the matrix biotite, to show Cl-rich composition and higher TiO_2 and X_{Mg} values than the retrograde ones.

Andalusite intergrown with biotite commonly replaces garnet (Fig. 2f-e). Retrograde andalusite is commonly accompanied by sillimanite and rare kyanite (Fig. 2e-n). Garnet is Fe-richer around the andalusite-bearing replacement, and andalusite in the replacement locally includes irregularly-shaped garnet and/or Zn-bearing spinel (Fig. 2k-n). Andalusite is never found as inclusions in garnet, and is in contact with the matrix phases even when it is surrounded by garnet (Fig. 2k-n).

Kyanite is rare, and tends to be finer-grained than other Al_2SiO_5 polymorphs and is never found as inclusions in garnet. It replaces garnet together with biotite, andalusite and sillimanite (Fig. 2g-j, m, n). The CL images combined with laser Raman spectroscopy are useful in identifying dispersed fine-grained kyanite because kyanite is more luminescent than sillimanite (moderately bright) and andalusite (dark) (Fig. 2g-j). Zn-bearing spinel is also found as inclusions in some kyanite grains.

The composition of Zn-bearing spinel included in all Al_2SiO_5 polymorphs and garnet varies from ZnO = 4.0-5.0 wt.% and X_{Mg} = 0.28 to ZnO = 11-13 wt.% and X_{Mg} = 0.18.

Garnet-biotite gneiss (sample 3001B)

This gneiss mainly consists of garnet, biotite, quartz, plagioclase and K-feldspar, with accessory zircon, ilmenite, fluorapatite and minor sulfide (Fig. 4a-c). Myrmekite is present in the matrix. Biotite included in garnet (Fig. 4a-c) shows high TiO_2 (3.5-7.3 wt.%) and moderate Cl (mostly 0.20-0.34 wt.%) contents and high X_{Mg} (~ 0.6) (Fig. 3c, d). Biotite in the matrix (Fig. 4a-c) has moderate TiO_2 (3.3-4.5 wt.%) and Cl (0.11-0.25 wt.%) contents and X_{Mg} of ~ 0.4 (Fig. 3c, d; Table 1). Retrograde biotite next to garnet, and crack-filling biotite in garnet (Fig. 4a-c) both show lower Cl contents below 0.21 wt.% (Fig. 3c, d). Some of the matrix biotite and retrograde biotites (in biotite-plagioclase intergrowths and retrograde biotite next to garnet) share the same chemical characteristics of having low TiO_2 and Cl contents and low X_{Mg} (Fig. 3c, d).

Garnet-biotite gneiss (sample 2601C)

This gneiss mainly consists of garnet, biotite, K-feldspar, quartz and plagioclase (Fig. 4d-f).

K-feldspar is abundant, and randomly-oriented secondary muscovite is present in the matrix. Accessory minerals are zircon, ilmenite and fluorapatite. Minor sulfide is included in garnet and minor myrmekite is locally present in the matrix. This sample has the most Fe-rich whole-rock composition among the samples studied as suggested by the Fe-rich composition of mafic minerals (X_{Mg} of biotite and garnet = 0.06-0.22; Table 1). Separate biotite grains in the matrix (Fig. 4d-f) show the highest Cl contents (0.61-0.68 wt.%) and the highest X_{Mg} (~ 0.2) in this sample (Figs. 3e, 3f and 4d-f). Biotite replacing garnet rim as biotite-plagioclase intergrowths (Fig. 4d-f) also show high X_{Mg} (~ 0.2) and moderate to high Cl content (0.32-0.41 wt.%) (Fig. 3e, f). It shares the same chemical characteristics as retrograde biotite near garnet. Crack-filling biotite in garnet (Fig. 4d-f) shows the lowest X_{Mg} and Cl contents (Fig. 3e, f). No systematic variation in TiO_2 content (2.2-3.8 wt.%) is observed among different biotite types in this sample (Fig. 3e, f).

LA-ICPMS U-Pb zircon dating

Zircon is commonly oval-shaped, and the diameter of zircon reported below represents the length of the shorter axis. Weighted mean and lower intercept ages given below are at 95% confidence level. Unless specified, ages reported below refer to $^{206}Pb/^{238}U$ results. A summary of the results of LA-ICPMS U-Pb zircon dating is given in Supplementary Table 2.

Sample 3001G

Zircon in the matrix is commonly shorter than 100 μm in diameter, and shows oscillatory zoning (Fig. 5a-h). Analyses gave concordant U-Pb ages of ca. 1200-1100 Ma, 950-900 Ma, 750-700 Ma and 650-550 Ma. Ages older than 700 Ma are in most cases obtained from zircon cores, and the youngest ages of ca. 580 Ma are in most cases obtained from rims. Ages older than 900 Ma tend to have high Th/U ratios from 0.20 up to 1.1, while the younger age domains (750-550 Ma) give low Th/U ratios below 0.20 (Figs. 5a-h and 6a; Table 2). The weighted mean U-Pb age of zircon rims from matrix grains is 581 ± 10 Ma (n = 5, mean square of weighted deviates (MSWD) = 1.3, probability = 0.28).

Zircon included in garnet is commonly about 50 μm in diameter, and tends to have oscillatory zoned cores with bright- and dark-CL zones (Th/U = 0.01-0.40, mostly around 0.25), discordantly overgrown by dark-CL rims (Th/U = 0.01-0.03) (Fig. 5e, h). The lower intercept age for selected rim analyses of zircon included in garnet is 578 ± 9 Ma (n = 6, MSWD = 1.3, probability = 0.28), and Th/U ratios of these zircon rims with concordant ages are 0.04-0.07. Rim and mantle of a zircon grain included in the inclusion-rich rim of a sillimanite porphyroblast yielded 575 ± 13 Ma (n = 2, Th/U = 0.04-0.09) (Fig. 5g).

Zircon in the garnet breakdown microstructure of Cl-poor Bt + Ms ± And shows similar zoning to zircon included in garnet (Fig. 5a-d). The weighted mean U-Pb age of zircon rims (and mantles with similar age) in such microstructure is 573 ± 5 Ma (n = 9, MSWD = 0.83, probability = 0.57).

Sample 3001B

Zircon in the matrix and zircon inclusions in garnet are commonly 30-70 µm in diameter, and shares similar microstructural features. The inherited core and mantle of zircon show oscillatory zoning under CL and BSE images, which are discordantly overgrown by relatively bright-CL rim (Figs. 5i-l, 6b). Zircon in this sample yielded concordant U-Pb ages of 850-700 Ma and 630-550 Ma (Fig. 6b). The youngest rim age from matrix zircon is 551 ± 14 Ma. Cores and rims of zircon included in garnet gave 758-585 Ma. Among them, the weighted mean of rims is 596 ± 7 Ma (n = 4, MSWD = 0.74, probability = 0.53). Both in the matrix zircon and inclusion zircon in garnet, domains of ca. 600 Ma commonly correspond to the bright-CL rim, and show high Th/U ratios up to 1.6 (Fig. 5i, j). However, some dark-CL parts with ca. 600 Ma age show relatively low Th/U ratios (0.05-0.38) (Fig. 5k).

Sample 2601C

Zircon in the matrix and included in garnet are commonly 60-100 µm and 20-70 µm in diameter, respectively (Fig. 5m-t). They share the same microstructural characteristics. The cores of zircon are oscillatory zoned and bright under CL image, or unzoned and dark (Fig. 5m-t). Several-µm to ca. 10 µm thick, bright-CL rims are commonly developed (Fig. 5m-t except for 5o). The oscillatory zoned cores tend to give older ages (> 600 Ma) than the unzoned dark-CL ones. Zircon in the matrix and inclusions in garnet both show concordant U-Pb ages of ca. 600-550 Ma (Figs. 5m-t, 6c). The weighted mean U-Pb age of the rims of zircon included in garnet is 583 ± 6 Ma (n = 17, MSWD = 1.14, probability = 0.31). No significant difference is observed between the age distribution patterns of matrix zircon and zircon inclusions in garnet. The Th/U ratios of zircon domains with 600-550 Ma ages are mostly below 0.40 (Figs. 5m-t, 6d).

Discussion

Pressure-temperature path of the pelitic gneiss from Perlebandet

Sample 3001G is strongly affected by retrograde metamorphism as suggested from the presence of retrograde andalusite and kyanite. Therefore, it is suitable for constraining the retrograde metamorphic *P-T* conditions. On the other hand, samples 2602D and 3001H are less affected by retrograde overprint, and thus used to estimate peak metamorphic conditions.

1. Prograde to peak metamorphic conditions

In all the sillimanite-bearing samples (3001G, 2602D and 3001H), sillimanite is commonly found as porphyroblasts in the matrix, and is considered to have been stable during peak metamorphism. The absence of prograde muscovite along the gneissose fabric together with the presence of sillimanite + K-feldspar in the matrix suggest that peak metamorphic conditions exceeded reaction (1)

$$Ms + Ab + Qtz \rightarrow Sil + Kfs + H_2O \text{ or melt.} \quad (1)$$

which was responsible for the formation of the core of sillimanite porphyroblasts in sample 3001G.

Sillimanite inclusions are abundant in garnet cores of samples 2602D and 3001H, and K-feldspar is also abundant in the matrix. Sillimanite in the matrix of sample 3001G is partly to completely overgrown by garnet (Fig. 2b-d), and some of the garnet overgrowths include Zn-bearing spinel grains (Fig. 2b-d), suggesting consumption of the sillimanite rims that are hosting spinel to form garnet with X_{Mg} = 0.10-0.20 (Fig. 7). Garnet with kyanite or andalusite inclusions is not seen in all studied samples. These are consistent with the progress of reaction (Fig. 7)

$$Sil + Bt + Qtz \rightarrow Grt + Kfs + \text{melt.} \quad (2)$$

The absence of cordierite in all garnet-bearing felsic gneiss samples suggests that the *P*-*T* conditions did not exceed the reaction

$$Bt + Sil + Qtz \rightarrow Grt + Crd + Kfs + \text{melt.} \quad (3)$$

Garnet, plagioclase, biotite and rare quartz are included in the inclusion-rich rim of a sillimanite porphyroblast in sample 3001G (Fig. 2b-d). The composition of biotite and garnet separately included in sillimanite (Table 1) are most likely to preserve compositions of entrapment, because sillimanite would hinder Fe-Mg exchange reactions between garnet and biotite after entrapment. Therefore, prograde *P*-*T* conditions can be estimated using these minerals. The Grt-Bt (GB) geothermometer (Holdaway et al., 1997; Holdaway, 2000) and the garnet-Al_2SiO_5-quartz-plagioclase (GASP) geobarometer (Holdaway, 2001) yielded ca. 700 °C, 0.47 GPa, which is in agreement within error of the geothermobarometry (± 50 °C and ± 0.10 GPa) with *P*-*T* conditions of reaction (2) for the observed garnet composition of X_{Mg}^{Grt} = 0.10-0.20 in the NaKFMASH system (Fig. 7). The rarity of quartz inclusions in the sillimanite rims may imply local absence of quartz, in which case the result may represent the highest-*P* estimate. Although the Grt-Bt thermometer of Holdaway (2000) does not account for the effects of F and Cl, calculations using the Zhu and Sverjensky (1992) calibration showed that the opposing effects of F (*T* increase) and Cl (*T* decrease) on the temperature estimate canceled each other out, and thus the effects of F and Cl are negligible in this sample.

On the other hand, the absence of a significant low-*P* retrograde overprint in samples 2602D and 3001H suggests that such rocks preserve peak metamorphic conditions better. In these samples, garnet core with sillimanite inclusions (Fig. 2a) and matrix plagioclase core are interpreted as coexisting with sillimanite and quartz, and used in the GASP geobarometry (Holdaway, 2000). For peak temperature estimate, Zr-in-rutile thermometry (Zack et al., 2004; Tomkins et al., 2007) was applied to rutile included in sillimanite and that in the matrix. The Tomkins et al. (2007) calibration is preferred in this study since it takes pressure effect into account and is experimentally calibrated. Peak *P*-*T* conditions estimated by the intersection of Zr-in-rutile thermometry (Tomkins et al., 2007) and GASP geobarometry (Holdaway, 2001) are ca. 768-840 °C and 0.8-1.0 GPa. The Grt-Bt geothermometry is considered less reliable than the Zr-in-rutile thermometry in this case, because the X_{Mg} of matrix biotite or inclusion biotite in garnet is more susceptible to retrograde re-equilibrium compared to rutile included in sillimanite. The peak *P-T* conditions above are consistent with those of reaction (2) for garnet with composition of $X_{Mg}^{Grt} \sim 0.40$, higher than that observed at the sillimanite-bearing garnet core (Table 1; Fig. 7), implying a modification of X_{Mg} of garnet during retrograde metamorphism.

Sample 3001G, affected by the low-*P* retrograde overprint, also preserves rutile as inclusions in garnet and K-feldspar or rarely in the matrix (Fig. 2o). The Zr-in-rutile thermometry gives temperature estimates (743-780 °C assuming 1.0 GPa) almost consistent with those of samples 2602D and 3001H. This observation strongly supports that sample 3001G shared the same peak *P-T* conditions as other samples before the low-*P* retrograde overprint.

2. Retrograde metamorphic conditions and proposed P-T path

In sample 3001G, peak garnet is commonly replaced by three Al_2SiO_5 polymorphs (Fig. 2i-j, m-n). It is difficult to define the sequence of andalusite and kyanite formation from their microtextures (Fig. 2g-j, m-n). Some sillimanite grains surrounding retrogressed garnet and including Zn-bearing spinel grains in sample 3001G (Fig. 2i) may have been originally included in garnet and survived the garnet breakdown reactions, because Zn-bearing spinel inclusions are the typical feature for prograde sillimanite rims (Fig. 2b, c). However, the coexistence of andalusite+sillimanite, andalusite+kyanite, and andalusite+kyanite+sillimanite in the replacement microtextures of garnet suggests garnet breakdown near the *P-T* conditions of the Al_2SiO_5 triple point. Since the coexistence of three Al_2SiO_5 polymorphs in the garnet breakdown microstructure is only preserved in sample 3001G, it is likely that localized fluid infiltrated this sample at *P-T* conditions of the Al_2SiO_5 triple point to trigger the retrograde reaction. This is also supported by the GASP geobarometry (Holdaway, 2000) and the Grt-Bt geothermometry (Holdaway et al., 1997; Holdaway, 2000) using mineral compositions of the breakdown microstructure of garnet into biotite, plagioclase, quartz and Al_2SiO_5 minerals, which yield *P-T* conditions of ca. 600 °C and 0.48 GPa, close to the Al_2SiO_5 triple point (Fig. 7). The almost complete cancelation of the opposite effects of F and Cl in biotite on the Grt-Bt geothermometer is confirmed by using Zhu and Sverjensky (1992) calibration, supporting the above *P-T* estimate. Since prograde (ca. 700 °C, 0.47 GPa) and retrograde (ca. 600 °C, 0.48 GPa) *P-T* conditions are estimated using the same geothermobarometers, and since the effects of F and Cl in biotite can be ignored, we consider the differences between them meaningful. Therefore, by connecting prograde, peak and retrograde *P-T* estimates from three samples, a counterclockwise *P-T* path for the Perlebandet rocks is proposed (Fig. 7).

Garnet rims are also locally replaced by the intergrowth of biotite and plagioclase in all samples. Utilizing the composition of garnet rims and biotite and plagioclase in the intergrowth, and applying the Grt-Bt geothermometer (Holdaway et al., 1997; Holdaway, 2000) and the garnet-biotite-plagioclase-quartz (GBPQ) geobarometer (Wu et al., 2004), retrograde *P-T* conditions of garnet breakdown to biotite + plagioclase are estimated. These vary depending on samples, and are ca. 580 °C and ca. 0.40 GPa for sample 3001G (average of 4 estimates; Fig. 7), ca. 640 °C, 0.66 GPa for sample 3001B (average of 5 estimates; Fig. 7), and ca. 760 °C, ca. 0.97 GPa for sample 2601C (average of 5 estimates; Fig. 7). Among these, an estimate from sample 3001G is consistent with the estimate by the GB-GASP pair (Fig. 7). These *P-T* conditions are consistent with the proposed counterclockwise *P-T* path (Fig. 7).

This proposed *P-T* path is very similar to that estimated for Brattnipene, central SRM (Fig. 1b; e.g., Adachi et al., 2013; Baba et al., 2013), suggesting that Perlebandet belongs to the SW terrane of the SRM (Fig. 1b; e.g., Mieth et al., 2014). Our results of zircon dating (Fig. 6) are consistent with previous results from Perlebandet (Shiraishi et al.. 2008) in that detrital ages older than 1200 Ma are absent. This is also true for SW terrane rocks of the SRM (Osanai et al., 2013), and thus zircon data also support Perlebandet as being part of the SW terrane (Fig. 1b).

Timings of Cl-bearing fluid infiltration and relationship with partial melting

The presence of Cl-rich biotite has been considered as evidence for the presence of brines (e.g., Newton et al., 1998; Manning and Aranovich, 2014; Safonov et al. 2014). Although the $f(H_2O)/f(HCl)$

ratio of the coexisting fluid can be deduced from the composition of biotite and apatite (e.g., Selby and Nesbitt, 2000), it should be noted that the salinity of the fluid cannot be directly determined by this method (e.g., Rubenach, 2005). However, if the fluid coexists with silicate melt, the HCl concentration can be related to the total Cl concentration in the fluid by the equation $\log(HCl/\Sigma Cl)^{aq}$ = -0.63-0.00035*P (bars) up to 0.67 GPa (Piccoli and Candela, 1994). This means that at pressures typical of the middle crust, most of the Cl forms complexes with cations other than H. Therefore, considering a case where Cl-bearing fluid coexists with melt, low $f(H_2O)/f(HCl)$ ratios in the fluid indicates abundant chloride salts in the fluid (i.e., high salinity). It is important, therefore, to carefully consider the melt-related processes that can increase Cl contents in biotite in addition to fluid-related processes. Several possible mechanisms to elevate Cl-contents in biotite are listed below, and their likeliness is discussed:

(a) Original Cl-rich whole-rock compositions allowed biotite to become Cl-rich.

(b) Consumption of originally Cl-bearing biotite through melting reactions caused an increase of Cl-content in remaining biotite.

(c) Retrograde consumption of H_2O by hydration reactions increased Cl content in the fluid, resulting in the increase of Cl in coexisting biotite (Kullerud, 1996; Markl and Bucher, 1998).

(d) Subsolidus Cl-rich fluid infiltration occurred (e.g., Newton et al., 1998; 2014; Higashino et al., 2015b).

(e) Infiltration of Cl-rich fluid triggered anatexis, and preferential partitioning of H_2O into the melt resulted in enrichment of Cl in the fluid (e.g., Aranovich et al., 2013; Safonov et al., 2014).

Cases (a)-(c) assume closed system behavior of Cl, and (d)-(e) assume open system behavior of Cl. Case (b) plays an important role if the partition coefficient of Cl between granitic melt and biotite is greater than 1. Based on experiments at 0.2 GPa, D_{Cl}(biotite/melt) is estimated to be ~1 to 6 (Icenhower and London, 1997). Recently, Safonov et al. (2014) performed a melting experiment of a biotite-amphibole gneiss with H_2O-CO_2-(K, Na)Cl fluids at 0.55 GPa and 750-800 °C. Their compositional data of coexisting biotite (X_{Mg} = 0.43-0.57) and melt imply that Cl is preferentially incorporated in the melt rather than in biotite, that is, D_{Cl}(biotite/melt) is less than 1 at 0.55 GPa and 800 °C. Therefore, the behavior of Cl under middle crustal depths can be different from that in shallow levels of the crust, and if this is the case, case (b) alone is not likely a strong process to elevate Cl content in biotite, at least for samples 3001B and 3001G having X_{Mg} values of biotite (X_{Mg} = 0.40-0.64; Table 1) similar to the experiment of Safonov et al (2014).

Sample 3001G preserves Cl-rich biotite (~ 0.4 wt.%) as inclusions in garnet. Biotite inclusions in garnet tend to re-equilibrate and change X_{Mg} on cooling, while preserving their original halogen content. Biotite was already Cl-rich prior to the garnet-formation by reaction (2), because moderately

Cl-bearing biotite (< 0.30 wt.%Cl) is included in sillimanite porphyroblasts predating garnet formation (Fig. 3a). Biotite inclusions in garnet from sample 3001B show the highest Cl-content in the sample, suggesting prograde formation of Cl-enriched biotite (Fig. 3b). Therefore, case (c) can be ruled out. Although case (a) cannot be ruled out, we consider that the similar timing of Cl-enriched biotite formation in different lithologies can be best explained by the infiltration of a Cl-rich fluid. The log[$f(H_2O)/f(HCl)$] and log[$f(H_2O)/f(HF)$] values of the fluid estimated assuming its presence during prograde stage for these two samples are in good agreement (Table 1), supporting the infiltration of fluids with a similar composition. External input of Cl-rich fluid is also supported by the localized field distribution of Cl-rich minerals in the SRM as discussed in the next section.

At P-T conditions estimated for reaction (2) in Perlebandet (~700 ºC and ~0.5 GPa), aH_2O of a pelitic gneiss undergoing partial melting can be estimated to be ~ 0.85 (Clemens and Vielzeuf, 1987). Ascribing this lowering of aH_2O to the addition of NaCl and KCl, XH_2O is estimated to be ~ 0.9 using the aH_2O-XH_2O relationship by Aranovich and Newton (1997), corresponding to ~ 26 wt% NaCl (KCl). This is the highest estimate of salinity of the fluid, because CO_2 can also contribute to lower aH_2O. It is difficult, however, to envisage source of the voluminous high-salinity fluid. More likely case is an infiltration of smaller volume of lower salinity fluids that continually increased salinity through preferential partitioning of H_2O into anatectic melts (Aranovich et al., 2013). In such case, we may assume that the fluid-present reaction such as follows (e.g., Yardley and Barber, 1991) took place prior to the dehydration melting reaction (2),

Bt + Sil + Kfs + Qtz + H_2O → melt (4).

As fluid-present melting reaction proceeds by consuming H_2O, log[$f(H_2O)/f(HCl)$] and log[$f(H_2O)/f(HF)$] values of the fluid will decrease, resulting in an increase of Cl content in biotite. Small volume of the fluid will be soon used up, resulting in cessation of the fluid-present partial melting reactions, and further melting must proceed by dehydration melting reactions (e.g., Brown, 2013) such as reaction (2) in the present case. The escape of concentrated fluids from the system with the assistance of deformation or low wetting angle of brines will also help switching the reaction from fluid-fluxed melting to dehydration melting. This process might explain why the Cl content of biotite included in peritectic garnet formed by dehydration melting reaction (2) is higher than that included in sillimanite porphyroblasts (Figs. 2b-d and 3).

On the other hand, some fluid-present melting reactions can also produce peritectic phases as sillimanite and garnet (Weinberg and Hasalová, 2015). Reactions such as

Ms + Pl + Qtz + H_2O → Sil + Bt + melt (5)

and

Bt ± Crd + Sil + Pl + Qtz + H_2O → Grt ± Kfs + melt (6)

(Jung et al., 2000; Milord et al., 2001) are the examples reported to occur at the *P*-*T* conditions for the beginning of partial melting in this study (~ 0.5 GPa and ~ 700 ºC). At medium pressure of ~ 0.5 GPa, fluid-present melting and dehydration melting reactions take place in relatively small temperature intervals. However, observed mineral compositions and sequences of reactions are mostly consistent with the *P-T* diagram constructed under the scheme of dehydration melting (Fig. 7). This might suggest that fluid-present melting occurred in the Perlebandet rocks only at the onset of the prograde partial melting process, and the subsequent melting occurred through dehydration melting reactions.

In sample 3001G, matrix biotite as a remnant of reaction (2) was presumably once Cl-rich. Compositional similarity between matrix biotite and microstructurally secondary biotite (Fig. 3) suggests that moderately Cl-bearing matrix biotite is a result of recrystallization of former Cl-rich biotite, re-equilibrated with retrograde fluids possibly released from the crystallizing melt. Using the *P-T* conditions of retrograde metamorphism, log[$f(H_2O)/f(HCl)$] of the retrograde fluid can be estimated as 4.2-4.3, with an average of 4.3 (Table 1).

The age of metamorphism and Cl-rich fluid infiltration

In sample 3001G, rims of matrix zircon and inclusion zircon in garnet and sillimanite all yielded U-Pb ages of 580-575 Ma. Most of these zircon rims show Th/U ratios below 0.1 (Fig. 6d), typical for metamorphic zircon (e.g., Rubatto, 2002). The garnet-forming reaction was probably partial melting reaction (2). Therefore, garnet-forming, sillimanite-grade metamorphism is likely to have occurred at or after ca. 580 Ma, together with the Cl-rich fluid infiltration. Moderately Cl-bearing biotite replacing garnet suggests that Cl-bearing aqueous fluid was present during retrograde garnet breakdown. The weighted mean U-Pb age of rims of zircon found in the microstructure of garnet replaced by Al_2SiO_5 minerals and biotite is 573 ± 5 Ma. The similarity of this age with zircon rims included in garnet implies that the retrogression took place soon after the peak metamorphism, or zircon was inert during the retrograde breakdown of garnet.

Samples 3001B and 2601C both give constraints that are consistent with the above scenario. For sample 3001B, the formation of garnet and moderately Cl-bearing biotite included in it (Fig. 3e, f) was presumably at 596 ± 7 Ma or younger. The fluid at retrograde stage shows log[$f(H_2O)/f(HCl)$] value of 4.0-5.0, with an average of 4.5 (Table 1). For sample 2601C, garnet growth would predate or coincide with 583 ± 6 Ma. Low Th/U zircon rims (Fig. 6d) supports this to be the metamorphic age. Markedly high Cl concentration of isolated matrix biotite in this sample (Cl > 0.61 wt.%) reflects Mg-Cl avoidance, in addition to the Cl-rich nature of the coexisted fluid, since biotite in this sample is Fe-richer than other samples (Fig. 3). The log[$f(H_2O)/f(HCl)$] of the near-peak to retrograde fluid is calculated as 3.5-4.2, with an average of 3.9 (Table 1).

To summarize, the timing of garnet-forming prograde metamorphism in Perlebandet is estimated to be ca. 580 Ma or younger. Since biotite was already enriched in Cl before the onset of reaction (2), the formation of highly to moderately Cl-bearing biotite in samples 3001G and 3001B took place before or at ca. 580 Ma during prograde metamorphism. Taking into account that estimated prograde log[f(H_2O)/f(HCl)] and log[f(H_2O)/f(HF)] of fluid are almost the same among the samples studied, it is likely that external Cl-bearing fluid infiltration occurred, prior to or simultaneously with the sillimanite-forming reaction. On the other hand, the presence of a retrograde, Cl-bearing fluid with log[f(H_2O)/f(HCl)] = 4.0-5.0 (with one exception of 3.5) is detected from three samples. This probably lasted until ca. 550 Ma. During the retrograde decompression, log[f(H_2O)/f(HCl)] of fluids increased slightly or was almost constant (Table 1; Fig. 7).

At the outcrop scale, fluid pathways may be localized (e.g., Aranovich et al., 2010; Dubinina et al., 2015; Kusebauch et al., 2015). This is also suggested in the SRM by localized distribution of post-peak Cl-rich veins in the outcrop scale in Brattnipene (Fig. 1b; Higashino et al., 2015b). The localized distribution of prograde Cl-bearing biotite in Perlebandet shows that Cl-bearing fluid pathways may be localized during prograde metamorphism as well, but obscured by later ductile deformation.

Comparison with other areas of the SRM

The *P-T-t* conditions of Cl-rich aqueous fluid infiltration in the SRM have been previously determined from two other localities; the eastern part (Balchenfjella; Higashino et al., 2013a) and the central part (Brattnipene; Higashino et al., 2015a) (Fig. 1b). In Balchenfjella, the *P-T* conditions of Cl-rich biotite and apatite entrapment in the garnet rim are estimated to be ca. 800°C and 0.80 GPa at

603 ± 14 Ma, which corresponds to the early retrograde stage postdating a peak metamorphic event at ca. 850^{o}C and 1.1 GPa (Higashino et al., 2013a). A subsequent Cl-poor fluid infiltration is recorded in Cl-poor matrix biotite, and estimated to have occurred at 564 ± 17 Ma from the rim age of zircon in the matrix (Higashino et al., 2013b). On the other hand, in Brattnipene, early retrograde Cl-rich fluid infiltration is estimated at ca. 700 ^{o}C, 0.75 GPa and after ca. 620 Ma (Higashino et al., 2015b). In contrast to these post-peak Cl-rich fluid activities, the present study shows that the Cl-rich biotite included in garnet was formed during prograde metamorphism possibly as a result of Cl-bearing fluid infiltration. External input of Cl-rich fluid during prograde- to peak-metamorphism possibly produced Cl-bearing partial melt, and its crystallization during decompression and cooling resulted in a release of post-peak, Cl-bearing fluid (Fig. 7).

Experimental data by Safonov et al. (2014) shows that melt can contain more Cl than coexisting biotite at 0.55 GPa and 750-800 ^{o}C. The fluid released by the crystallization of such melt would have significantly more Cl than coexisting melt (Webster, 1992; Aranovich et al., 2013). Therefore, one possible mechanism to produce Cl-rich fluid during the retrograde stage is the crystallization of Cl-bearing partial melt. However, if the partial melting and crystallization of the melt alone is the cause of Cl-rich fluid, Cl-rich biotite should be more widely distributed throughout the NE terrane of the SRM where partially molten granulites and migmatites are widely distributed (Fig. 1b). What is actually observed in the field is the localized distribution of Cl-rich biotite and hornblende along large-scale shear zones and detachments both in felsic and mafic gneisses (Fig. 1b; Higashino et al., 2015a). The distribution of Cl-rich minerals corresponds with the boundaries of magnetic anomaly domains of Mieth et al. (2014). This trend may be obscured by a possible granite intrusion near Perlebandet that is inferred to be the source of a high-magnetic anomaly (Mieth et al., 2014), but ignoring the possible effect of this granite intrusion, Perlebandet is also located along the boundaries of magnetic anomaly domains which corresponds to the major tectonic boundaries (e.g., Mieth et al. 2014). These suggest that the input of Cl in the SRM including Perlebandet is probably external, possibly as Cl-rich fluid infiltration channeled along the tectonic boundaries (e.g., Glassley et al., 2010) during prograde metamorphism. One occurrence of Cl-rich biotite in Brattnipene is at a major shear zone containing peridotite and pyroxenite lenses (Fig. 1b; location 4 of Higashino et al. 2013), supporting this idea. Because Perlebandet and Brattnipene share the counterclockwise *P*-*T* paths, they should both belong to the footwall side of the MTB based on the tectonic model by Osanai et al. (2013) (Fig. 8). Therefore, the Cl-rich fluid infiltration presumably took place at the uppermost part of the footwall of the MTB (Fig. 8).

Based on this tectonic constraint, there are several candidates for the origin of the Cl-rich fluids. Because the Mozambique Ocean is considered to have been located between the NE and SW terranes of the SRM before collision (Otsuji et al., 2016), sea water introduced into the depth and fluids released from the mantle are the likely candidates, and should be examined in future studies. High Cl content in biotite, hornblende and apatite is a measure of low log[$f(H_2O)/f(HCl)$] of fluids, implying that the origin of Cl-rich fluids in the SRM can be also related to the magmatic activity during collision.

Multiple episodes of zircon growth within single orthogneissic samples from the NE terrane with ages from ca. 630 Ma to ca. 535 Ma described by Grantham et al. (2013) and the result of this study from the SW terrane indicate a long history of metamorphism, magmatism and deformation that affected both terranes (e.g., Elburg et al., 2016), and multiple Cl-rich fluid infiltrations took place in the SRM during this period (e.g., Higashino et al., 2013; 2015a).

Conclusion

Chlorine-rich fluid infiltration into the upper-amphibolite- to granulite-facies middle continental crust at the prograde stage of counterclockwise *P-T* path is likely at Perlebandet (western SRM, East Antarctica). This presumably occurred in the uppermost part of the footwall of the continental collision boundary at ca. 580 Ma. The localized distribution of Cl-rich biotite and hornblende along large-scale shear zones and detachments in the SRM supports the external input of Cl-rich fluids through tectonic boundaries during continental collision.

Acknowledgements

We would like to thank R.C. Newton and L.Y. Aranovich for constructive reviews that helped improving the manuscript and M. Scambelluri for editorial efforts. D. van Reenen is thanked for critical comments on the previous version of the manuscript. Members of JARE and Nishi-Higashi seminar are thanked for fruitful discussions and supports during the field work in the SRM. Kota Takatsuka and Kentaro Hattori are thanked for assistance during LA-ICPMS analyses. This study was financially supported by the JSPS KAKENHI Grant Number 26400513 and the NIPR General Collaboration Project (No.25-14) to T. Kawakami, and Grant-in-Aid for JSPS Fellows (No. 25・715) to F. Higashino.

References

Adachi, T., Hokada, T., Osanai, Y., Nakano, N., Baba, S., Toyoshima, T., 2013. Contrasting metamorphic records and their implications for tectonic process in the central Sør Rondane Mountains, eastern Dronning Maud Land, East Antarctica. In: Harley SL, Fitzsimons LCW, Zhao Y (ed) Antarctica and Supercontinent Evolution. Geological Society, London, Special Publication 383, 113-133.

Aranovich, L.Y., Shmulovich, K.I., Fedkin, V.V., 1987. The H_2O and CO_2 regime in regional metamorphism. International Geology Review 29, 1379-1401.

Aranovich, L.Y., Dubinina, E.O., Avdeenko, A.S., Lebedeva, Y.M., Bushmin, S.A., Dolivo-Dobrovol'skii, D.D., 2010. Oxygen isotopic composition of coexisting minerals of sillimanite-hypersthene rocks from the Por'ya bay area: Evidence of fluid involvement in granulite-facies metamorphism. Geochemistry International 48, 739-751.

Aranovich, L.Y., Newton, R.C., Manning, C.E., 2013. Brine-assisted anatexis: Experimental melting in the system haplogranite–H_2O–NaCl–KCl at deep-crustal conditions. Earth and Planetary Science Letters 374, 111-120.

Asami, M., Shiraishi, K., 1987. Kyanite from the western part of the Sør Rondane Mountains, East Antarctica. Proceedings of the NIPR symposium on Antarctic Geosciences 1, 150-168.

Asami, M., Osanai, Y., Shiraishi, K., Makimoto, H., 1992. Metamorphic evolution of the Sør Rondane Mountains, East Antarctica. In: Yoshida, Y., Kaminuma, K., Shiraishi, K. (Eds.), Recent Progress in Antarctic Earth Science. Terra Scientific Publishing Company, Tokyo, pp. 7–15.

Baba, S., Osanai, Y., Nakano, N., Owada, M., Hokada, T., Horie, K., Adachi, T., Toyoshima, T., 2013. Counterclockwise P–T path and isobaric cooling of metapelites from Brattnipene, Sør Rondane Mountains, East Antarctica: Implications for a tectonothermal event at the proto-Gondwana margin. Precambrian Research 234, 210–228.

Brown, M., 2013. Granite: From genesis to emplacement. GSA Bulletin 125, 1079–1113.

Dubinina E.O., Aranovich, L.Y., van Reenen, D.D., Avdeenko, A.S., Varlamov, D.A., Shaposhnikov, V.V., Kurdyukov, E.B., 2015. Involvement of fluids in the metamorphic processes within different zones of the Southern Marginal Zone of the Limpopo complex, South Africa: An oxygen isotope perspective. Precambrian Research 256, 48-61.

Elburg, M.A., Andersen, T., Jacobs, J., Läufer, A., Ruppel, A., Krohne, N., Damaske, D., 2016. One Hundred Fifty Million Years of Intrusive Activity in the Sør Rondane Mountains (East Antarctica): Implications for Gondwana Assembly. The Journal of Geology 124, 1-26.

Glassley, W.E., Korstgårda, J.A., Sørensen, K., 2010. K-rich brine and chemical modification of the crust during continent–continent collision, Nagssugtoqidian Orogen, West Greenland. Precambrian Research 180, 47–62.

Goldoff, B., Webster, J.D., Harlov, D.E., 2012. Characterization of fluor-chlorapatites by electron probe microanalysis with a focus on time-dependent intensity variation of halogens. American Mineralogist 97, 1103-1115.

Grantham, G.H., Macey, P.H., Ingram, B.A., Roberts, M.P. Armstrong, R.A., Hokada, T., Shiraishi, K., Jackson, C., Bisnath A., Manhica V., 2008. Terrane correlation between Antarctica, Mozambique and Sri Lanka; comparisons of geochronology, lithology, structure and metamorphism and possible implications for the geology of southern Africa and Antarctica..Geological Society, London, Special Publications 308, 91-119.

Grantham, G.H., Macey, P.H., Horie, K., Kawakami, T., Ishikawa, M., Satish-Kumar, M., Tsuchiya, N., Graser, P., Azevedo, S., 2013. Comparison of the metamorphic history of the Monapo

Complex, northern Mozambique and Balchenfjella and Austhameren areas Sør Rondane, Antarctica: Implications for the Kuunga Orogeny and the amalgamation of N and S. Gondwana. Precambrian Research 234, 85–135.

Grew, E.S., Asami, M., Makimoto, H., 1989. Preliminary petrological studies of the metamorphic rocks of the eastern Sør Rondane Mountains. Proceedings of the NIPR symposium on Antarctic Geosciences 3, 100-127.

Harlov, D.E., Förster, H.J., 2002. High-grade fluid metasomatism on both a local and a regional scale: the Seward Peninsula, Alaska, and the Val Strona di Omegna, Ivrea-Verbano Zone, northern Italy. Part 1: Petrography and silicate mineral chemistry. Journal of Petrology 43, 769-799.

Heinrich, W., 2007. Fluid immiscibility in metamorphic rocks. Fluid-fluid interactions. Reviews in Mineralogy and Geochemistry 65, 389-430.

Higashino, F., Kawakami, T., Satish-Kumar, M., Ishikawa, M., Maki, K., Tsuchiya, N., Grantham, G.H., Hirata, T., 2013a. Chlorine-rich fluid or melt activity during granulite facies metamorphism in the Late Proterozoic to Cambrian continental collision zone- An example from the Sør Rondane Mountains, East Antarctica. Precambrian Research 234, 229-246.

Higashino, F., Kawakami, T., Satish-Kumar, M., Ishikawa, M., Tsuchiya, N., Grantham, G.H., 2013b. Multi-stage Cl-rich fluid activity and behavior of REE-bearing minerals in a Neoproterozoic granulite terrane. Goldschmidt 2013 abstract, Mineralogical Magazine 77, 1298.

Higashino, F., Kawakami, T., Tsuchiya, N., Satish-Kumar, M., Ishikawa, M., Grantham, G.H., Sakata, S., Hattori, K., Hirata, T., 2015a. Geochemical behavior of zirconium during Cl-rich aqueous fluid infiltration under upper amphibolite facies metamorphism – A case study from Brattnipene, Sør Rondane Mountains, East Antarctica. Journal of Mineralogical and Petrological Sciences 110, 166-178.

Higashino, F., Kawakami, T., Tsuchiya, N., Satish-Kumar, M., Ishikawa, M., Grantham, G.H., 2015b. Mass transfer in mafic gneiss during upper-amphibolite facies chloride brine infiltration. Goldschmidt 2015 abstract, 1268.

Hiroi Y., Yanagi A., Kato M., Kobayashi T., Prame B., Hokada T., Satish-Kumar M., Ishikawa M., Adachi, T., Osanai Y., Motoyoshi Y., Shiraishi GK., 2014. Supercooled melt inclusions in lower-crustal granulites as a consequence of rapid exhumation by channel flow. Gondwana Research 25, 226–234.

Holdaway, M.J., 2000. Application of new experimental and garnet Margules data to the garnet–biotite geothermometer. American Mineralogist 85, 881–892.

Holdaway, M.J., 2001. Recalibration of the GASP geobarometer in light of recent garnet and plagioclase activity models and versions of the garnet-biotite geothermometer. American Mineralogist 86, 1117-1129.

Holdaway, M.J., Mukhopadhyay, B., Dyar, M.D., Guidotti, C.V., Dutrow, B.L., 1997. Garnet-biotite geothermometry revised: New Margules parameters and a natural specimen data set from Maine. American Mineralogist 82, 582-595.

Holness, M.B., 1997. Surface chemical controls on pore-fluid connectivity in texturally equilibrated materials. In: Jamtveit, B., Yardley, B.W.D. (Eds.), Fluid Flow and Transport in Rocks. Chapman and Hall, London, pp. 149–169.

Holness, M.B., Cesare, B., Sawyer, E.W., 2011. Melted rocks under the microscope: Microstructures and their interpretation. Elements 7, 247–252.

Ishikawa, M., Kawakami, T., Satish-Kumar, M., Grantham, G.H., Hokazono, Y., Saso, M., Tsuchiya, N., 2013. Late Neoproterozoic extensional detachment in eastern Sør Rondane Mountains, East Antarctica: Implications for the collapse of East African Antarctic Orogen. Precambrian Research 234, 247-256.

Icenhower, J., London, D., 1997. Partitioning of fluorine and chlorine between biotite and granitic melt: experimental calibration at 200 MPa H_2O. Contributions to Mineralogy and Petrology 127, 17-29.

Jacobs, J., Bauer, W., Fanning, C.M., 2003. Late Neoproterozoic/Early Palaeozoic events in central Dronning Maud Land and significance for the southern extension of the East African Orogen into East Antarctica. Precambrian Research 126, 27-53.

Jacobs, J., Elburg, M., Läufer, A., Kleinhanns, I.C., Henjes-Kunst, F., Estrada, S., Ruppel, A.S., Damaske, D., Montero, P., Bea, F., 2015. Two distinct Late Mesoproterozoic/Early Neoproterozoic basement provinces in central/eastern Dronning Maud Land, East Antarctica: The missing link, 15–21°. Precambrian Research 265, 249-272.

Jung, S., Hoernes, S., Mezger, K., 2000. Geochronology and petrology of migmatites from the Proterozoic Damara Belt — importance of episodic fluid-present disequilibrium melting and consequences for granite petrology. Lithos 51, 153–179.

Kamei A., Horie K., Owada M., Yuhara M., Nakano N., Osanai Y., Adachi T., Hara Y., Terao M., Teuchi S., Shimura T., Tsukada K., Hokada T., Iwata C., Shiraishi K., Ishizuka H., Takahashi Y., 2013. Late Proterozoic juvenile arc metatonalite and adakitic intrusions in the Sør Rondane Mountains, Eastern Dronning Maud Land, Antarctica. Precambrian Research 234, 47-62.

Kawakami, T., Hokada, T., Sakata, S., Hirata, T., 2016. Possible polymetamorphism indicated by monazite and zircon dating and isotope mapping of garnet, and significance of Cl-rich biotite coexisted with melt in the garnet-sillimanite gneiss, Skallevikshalsen, Lützow-Holm Complex, East Antarctica. Journal of Mineralogical and Petrological Science 111, 129-143.

Kawakami, T., Satish-Kumar, M., Tsuchiya, N., Ishikawa, M., Higashino, F., Grantham, G.H., Yoshida, K., 2010. Pelitic metamorphic rocks from Perlebandet and Balchenfjella, Sør Rondane Mountains, East Antarctica. Abstract of the First Symposium on Polar Science. GO008.

Kitano, I., Osanai, Y., Nakano, N., Adachi, T., 2016. Detrital zircon provenances for metamorphic rocks from southern Sør Rondane Mountains, East Antarctica: A new report of Archean to Mesoproterozoic zircons. Journal of Mineralogical and Petrological Science 111, 118-128.

Kojima, S., Shiraishi, K., 1986. Note on the geology of the western part of the Sør Rondane Mountains, East Antarctica. Memoirs of National Institute of Polar Research, Special Issue, 43, 116-132.

Kretz, R., 1983. Symbols for rock-forming minerals. American Mineralogist 68, 277-279.

Kullerud, K., 1996. Chlorine-rich amphiboles: interplay between amphibole composition and an evolving fluid. European Journal of Mineralogy 8, 355-370.

Kusebauch, C., John, T., Barnes, J.D., Klügel, A., Austrheim, H.O., 2015. Halogen element and stable chlorine isotope fractionation caused by fluid–rock interaction (Bamble Sector, SE Norway). Journal of Petrology 56, 299-324.

Li, Z., Tainosho, Y., Shiraishi, K., Owada, M., 2003. Chemical characteristics of fluorine-bearing biotite of early Paleozoic plutonic rocks from the Sør Rondane Mountains, East Antarctica. Geochemical Journal 37, 145–161.

Li, Z., Du, Z., Yang, S., Chen, H., Song, B., Liu, D., 2006. First report of zircon SHRIMP U–Pb dating from the Dufek granite in the Sør Rondane Mountains, East Antarctica. Journal of Zhejiang University Science A (Suppl. II), 315–319.

Li, Z.L., Chen, H., Yang, S., Tainosho, Y., Shiraishi, K., Owada, M., 2007. Fluid components in accessory minerals of Pan-African granitoids in the Sør Rondane Mountains, East Antarctica. Journal of Zhejiang University Science A 8, 1004-1010.

Ludwig, K.R., 2012. User's manual for Isoplot 3.75. A geological toolkit for Microsoft Excel. Berkeley Geochronology Center Special Publication No.5 (revision of January 30, 2012. 75 pp.).

Manning, C.E., Aranovich, L.Y., 2014. Brines at high pressure and temperature: Thermodynamic, petrologic and geochemical effects. Precambrian Research 253, 6-16.

Markl, G., Bucher, K., 1998. Composition of fluids in the lower crust inferred from metamorphic salt in lower crustal rocks. Nature 391, 781-783.

Mathez, E.A., Webster, J.D., 2005. Partitioning behavior of chlorine and fluorine in the system apatite-melt-fluid. Geochimica et Cosmochimica Acta 69, 1275-1286.

Meert, J., 2003. A synopsis of events related to the assembly of eastern Gondwana. Tectonophysics 362, 1–40.

Mieth, M., Jacobs, J., Ruppel, A., Damaske, D., Läufer, A., Jokat, W., 2014. New detailed aeromagnetic and geological data of eastern Dronning Maud Land: Implications for refining the tectonic and structural framework of Sør Rondane, East Antarctica. Precambrian Research 245, 174-185.

Milord, I., Sawyer, E.W., Brown, M., 2001. Formation of diatexite migmatite and granite magma during anatexis of semi-pelitic metasedimentary rocks: an example from St. Malo, France. Journal of Petrology 42, 487-505.

Munoz, J.L., Swenson, A., 1981. Chrolide-hydroxyl exchange in biotite and estimation of relative HCl/HF activities in hydrothermal fluids. Economic Geology 76, 2212-2221.

Munoz, J.L., 1992. Calculation of HF and HCl fugacities from biotite compositions: revised equations. Geological Society of America, Abstract with Programs 24, A221.

Newton, R.C., Aranovich,L.Y., Hansen,E.C., Vandenheuvel,B.A., 1998. Hypersaline fluids in Precambrian deep-crustal metamorphism. Precambrian Research 91, 41-63.

Newton, R.C., Touret, J.L.R., Aranovich, L.Y., 2014. Fluids and H_2O activity at the onset of granulite facies metamorphism. Precambrian Research 253, 17-25.

Osanai, Y., Shiraishi, K., Takahashi, Y., Ishizuka, H., Tainosho, Y., Tsuchiya, N., Sakiyama, T., Kodama, S., 1992. Geochemical characteristics of metamorphic rocks from the central Sør Rondane Mountains, East Antarctica. In: Yoshida, Y., Kaminuma, K., Shiraishi, K. (Eds.), Recent Progress in Antarctic Earth Science. Terra Scientific Publishing Company, Tokyo, pp. 17–27.

Osanai, Y., Nogi, Y., Baba, S., Nakano, N., Adachi, T., Hokada, T., Toyoshima, T., Owada, M., Satish-Kumar, M., Kamei, A., Kitano, I., 2013. Geologic evolution of the Sør Rondane Mountains, East Antarctica: Collision tectonics proposed based on metamorphic processes and magnetic anomalies. Precambrian Research 234, 8-29.

Otsuji, N., Satish-Kumar, M., Kamei, A., Tsuchiya, N., Kawakami, T., Ishikawa, M., Grantham, G. H., 2013. Late-Tonian to early-Cryogenian apparent depositional ages for metacarbonate rocks from the Sør Rondane Mountains, East Antarctica. Precambrian Research 234, 257-278.

Otsuji, N., Satish-Kumar, M., Kamei, A., Takazawa, E., Tsuchiya, N., Grantham, G. H., Kawakami, T., Ishikawa, M., Osanai, Y., 2016. Sr and Nd Isotopic evidence in metacarbonate rocks for an extinct Island arc - ocean system in East Antarctica. Journal of Mineralogical and Petrological Sciences 111, 170-180.

Piccoli, P., Candela, P., 1994. Apatite in felsic rocks: a model for the estimation of initial halogen concentrations in the Bishop Tuff (Long Valley) and Tuolumne intrusive suite (Sierra Nevada Batholith) magmas. American Journal of Science 294, 92-135.

Rubatto, D., 2002. Zircon trace element geochemistry: partitioning with garnet and the link between U–Pb ages and metamorphism. Chemical Geology 184, 123-138.

Rubenach, M.J., 2005. Relative timing of albitization and chlorine enrichment in biotite in Proterozoic schists, Snake Creek anticline, Mount Isa inlier, Northeastern Australia. The Canadian Mineralogist 43, 349-366.

Ruppel, A.S., Läufer, A., Jacobs, J., Elburg, M., Krohne, N., Damaske, D., Lisker, F., 2015. The Main Shear Zone in Sør Rondane, East Antarctica: Implications for the late-Pan-African tectonic evolution of Dronning Maud Land. Tectonics 34, 1290-1305.

Safonov, O.G., Kosova, S.A., Van Reenen, D.D., 2014. Interaction of biotite-amphibole gneiss with H_2O-CO_2-(K, Na)Cl fluids at 550MPa and 750 and 800ºC: Experimental study and applications to dehydration and partial melting in the middle crust. Journal of Petrology 55, 2419-2456.

Selby, D., Nesbitt, B.E., 2000. Chemical composition of biotite from the Casino porphyry Cu-Au-Mo mineralization, Yukon, Canada: evaluation of magmatic and hydrothermal fluid chemistry. Chemical Geology 171, 77-93.

Shiraishi, K., Kojima, S., 1987. Basic and intermediate gneisses from the western part of the Sør Rondane Mountains, East Antarctica. Proceedings of the NIPR symposium on Antarctic Geosciences 1, 129-149.

Shiraishi, K., Asami, M., Ishizuka, H., Kojima, H., Kojima, S., Osanai, Y., Sakiyama, T., Takahashi, Y., Yamazaki, M., Yoshikura, S., 1991. Geology and metamorphism of the Sør Rondane Mountains, East Antarctica. In: Thomson, M.R.A., Crame, J.A., Thomson, J.W. (Eds.), Geological Evolution of Antarctica. Cambridge University Press, Cambridge, pp. 77–82.

Shiraishi, K., Osanai, Y., Tainosho, Y., Takahashi, Y., Tsuchiya, N., Kojima, S., Yanai, K., Moriwaki, K., 1992. Geological map of Widerøefjellet. Antarctic Geological Map Series, sheet 32, scale 1:100,000, National Institute of Polar Research, Tokyo.

Shiraishi, K., Osanai, Y., Ishizuka, H., Asami, M., 1997. Geological map of the Sør Rondane

Mountains, Antarctica. Antarctic Geological Map Series, sheet 35, scale 1:250,000, National Institute of Polar Research, Tokyo.

Shiraishi, K., Dunkley, D.J., Hokada, T., Fanning, C.M., Kagami, H., Hamamoto, T., 2008. Geochronological constrains on the Late Proterozoic to Cambrian crustal evolution of eastern Dronning Maud Land, East Antarctica: a synthesis of SHRIMP U-Pb age and Nd model age data. Geological Society of London, Special Publications 308, 21–67.

Spear, F.S., Kohn, M.J., Cheney, J.T., 1999. P-T paths from anatectic pelites. Contributions to Mineralogy and Petrology 134, 17-32.

Tomkins, H.S., Powell, R., Ellis, D.J., 2007. The pressure dependence of the zirconium-in-rutile thermometer. Journal of metamorphic Geology 25, 703-713.

Touret, J.L.R., Huizenga, J.M., 2011. Fluids in granulites. The Geological Society of America Memoir 207, 25-37.

Touret, J.L.R., Santosh, M., Huizenga, J.M., 2016. High-temperature granulites and supercontinents. Geoscience Frontiers 7, 101-113.

Toyoshima, T., Osanai, Y., Baba, S., Hokada, T., Nakano, N., Adachi, T., Otsubo, M., Ishikawa, M., Nogi, Y., 2013. Sinistral transpressional and extensional tectonics in Dronning Maud Land, East Antarctica, including the Sør Rondane Mountains. Precambrian Research 234, 30-46.

Tsuchiya, N., Ishikawa, M., Satish-Kumar, M., Kawakami, T., Kojima, H., Kaiden, H., Miura, H., Suganuma, Y., Abe, M., Sasaki, D., Chiba, M., Okada, Y., Hashizume, F., Grantham, G., Goderis, S., 2012. Report on geological fieldwork in the Sør Rondane Mountains, Eastern Dronning Maud Land, 2009–2010 (JARE-51). Antarctic Record 56, 295–379.

Van den Berg, R., Huizenga, J.M., 2001. Fluids in granulites of the Southern Marginal Zone of the Limpopo Belt, South Africa. Contributions to Mineralogy and Petrology 141, 529-545.

Watson, E.B., Brenan, J.M., 1987. Fluids in lithosphere, 1. Experimentally determined wetting characteristics of CO_2-H_2O fluids and their implications for fluid transport, host-rock physical properties and fluid inclusion formation. Earth and Planetary Science Letters 85, 594–615.

Webster, J.D., 1992. Fluid-melt interactions involving Cl-rich granites: Experimental study from 2 to 8 kbar. Geochimica et Cosmochimica Acta 56, 659-678.

Weinberg, R.F., Hasalová, P., 2015. Water-fluxed melting of the continental crust: A review. Lithos 212-215, 158-188.

Wu, C.-M., Zhang, J., Ren, L.-D., 2004. Empirical garnet-biotite-plagioclase-quartz (GBPQ) geobarometry in medium- to high-grade metapelites. Journal of Petrology 45, 1907-1921.

Yardley, B.W.D., Barber, J.P., 1991. Melting reactions in the Connemara Schists: the role of water infiltration in the formation of amphibolite facies migmatites. American Mineralogist 76, 848–856.

Zack, T., Moraes, A.R., Kronz, A.A., 2004. Temperature dependence of Zr in rutile: empirical calibration of a rutile thermometer. Contributions to Mineralogy and Petrology 148, 471-488.

Zhu, C., Sverjensky, D.A., 1991. Partitioning of F-Cl-OH between minerals and hydrothermal fluids. Geochimica et Cosmochimica Acta 55, 1837-1858.

Zhu, C., Sverjensky, D.A., 1992. F-Cl-OH partitioning between biotite and apatite. Geochimica et Cosmochimica Acta 56, 3435-3467.

Figure captions

Figure 1. (a) Gondwana amalgamation model by Neoproterozoic orogens. East African Orogen and Kuunga Orogen (Meert, 2003) are shown. Position of the Sør Rondane Mountains is shown by a star. (b) Geological map of the Sør Rondane Mountains, East Antarctica (modified after Shiraishi et al., 1997, 2008; Osanai et al., 1992; 2013; Toyoshima et al., 2013; Ishikawa et al., 2013), showing the location of Perlebandet. Chlorine concentrations of biotite (circles) and amphibole (squares) in pelitic and mafic gneisses (Higashino et al., 2013a; 2015a) are also shown. Warm color represents biotite or hornblende with higher-Cl contents. Note that Cl-rich biotite and hornblende are localized near tectonic boundaries and shear zones. location 4; location 4 of Higashino et al. (2013). The Main Tectonic Boundary (O) is after Osanai et al. (2013) and the Main Tectonic Boundary (M) is after Mieth et al. (2014). (c) Geological map of Perlebandet after Shiraishi et al. (1992). Sample localities are also shown.

Figure 2. (a) Garnet porphyroblast including abundant sillimanite needles in the core. Sillimanite is also arranged along the gneissose structure of the matrix (top). Sample 2602D. Plane polarized light (PPL). (b)-(o) Mode of occurrence of metamorphic minerals in a garnet-sillimanite-biotite gneiss (sample 3001G). (b) Sillimanite including Zn-bearing spinel overgrown by garnet. This microstructure is interpreted to represent staurolite breakdown. Crossed polarized light (CPL). (c) Sillimanite porphyroblast with the inclusion-poor core and inclusion-rich rim. Subgrain boundaries can be clearly observed. CPL. (d) Enlargement of the dotted square in (c). Zn-bearing spinel is included in the inclusion-rich rim of the sillimanite porphyroblast. Cl-rich biotite and ilmenite are included in the inclusion-poor core of the sillimanite. PPL. (e) Sillimanite, andalusite and biotite replacing garnet. PPL. (f) Garnet rim replaced by biotite + andalusite intergrowth with minor fibrolitic sillimanite. PPL. (g) BSE image of breakdown microstructure of garnet replaced by biotite, plagioclase, andalusite + quartz intergrowth, kyanite and muscovite. Outlines of kyanite grains are indicated by red lines. (h) Panchromatic CL image of the same area as (g). Warm colors indicate higher CL intensity. Note the high CL intensity of kyanite compared to low CL intensity of andalusite. (i) BSE image of breakdown microstructure of garnet replaced by biotite, plagioclase, quartz, andalusite, kyanite and sillimanite. Sillimanite includes Zn-bearing spinel grains. Outline of kyanite grains are indicated by red lines. (j) Panchromatic CL image of the same area as (i).

Warm colors indicate higher CL intensity. Note the high CL intensity of kyanite compared to moderate and low intensity of sillimanite and andalusite, respectively. (k) Garnet including sillimanite and Zn-bearing spinel, which is partly replaced by the aggregate of Bt + And + Sil + Crn + Spl + Ms at the rim. PPL. (l) CPL of (k). Sillimanite is separately included in garnet, whereas andalusite and sillimanite are found in the replacement microstructure of garnet. (m) Garnet that is including Zn-bearing spinel is partly replaced by the retrograde aggregate of Bt + And + Ky + Sil + Spl. PPL. (n) CPL of (m). Note that andalusite and kyanite (right), as well as andalusite and sillimanite (center) are in direct contact. (o) A BSE image of rutile partly replaced by ilmenite. Both of them are included in garnet.

Figure 3. Plots showing the variations of biotite composition depending on the mode of occurrence. (a) TiO_2 (wt.%) vs X_{Mg} plot for sample 3001G. (b) Cl (wt.%) vs X_{Mg} plot for sample 3001G. (c) TiO_2 (wt.%) vs X_{Mg} plot for sample 3001B. (d) Cl (wt.%) vs X_{Mg} plot for sample 3001B. (e) TiO_2 (wt.%) vs X_{Mg} plot for sample 2601C. (b) Cl (wt.%) vs X_{Mg} plot for sample 2601C.

Figure 4. X-ray elemental mappings and BSE images showing the mode of occurrence of Cl-rich biotite from samples 3001B (a-c) and 2601C (d-f). (a) BSI of garnet including Cl-rich biotite and apatite. Garnet is partly replaced by retrograde biotite at the rim and along the cracks. (b) X-ray elemental map of Cl for the area including (a). Cl-rich biotite (yellow to yellowish green) is present as inclusions in garnet and as a matrix phase (especially at the top of the map).

Retrograde biotite replacing garnet has lower Cl content (light blue). Apatite included in garnet is enriched in Cl. (c) X-ray elemental map of Mg for the same area as (b). Some of the Cl-rich biotite grains included in garnet show higher Mg content (red) than the matrix biotite (greenish yellow). (d) BSI of garnet partly replaced by biotite-plagioclase intergrowths. (e) X-ray elemental maps of Cl for the area including (d). Cl-rich biotite is present as an isolate matrix phase (yellowish green). Moderately Cl-bearing biotite is present as a biotite-plagioclase intergrowth replacing garnet (light blue). (f) X-ray elemental map of Mg for the same area as (d).

Figure 5. CL images of zircon from Perlebandet. (a)-(h) Sample 3001G. (i)-(l) Sample 3001B. (m)-(t) Sample 2601C. Red circles represent the pits of the LA-ICPMS U-Pb dating (5 μm) and numbers given are the $^{206}Pb/^{238}U$ age ± 2S.D. error [better than 95-105% concordance, where concordance = ($^{206}Pb/^{238}U$ age)*100/($^{207}Pb/^{235}U$ age)] and Th/U ratio. *in Grt bd*; zircon present in garnet breakdown microstructure developed around garnet. *matrix*; zircon present in the matrix. *in Grt/Sil rim*; zircon included in garnet/sillimanite rim. *** Ma; discordant data point.

Figure 6. (a)-(c) Concordia diagrams and probability density plot (inset) for the LA-ICPMS U-Pb zircon dating. Concordant data (concordance = 95-105%) are used to construct the probability density plot. Color variation of the error ellipses represents Th/U ratio of the dated spots. Note that ages older than ca. 1200 Ma is absent in all samples. (a) Sample 3001G. (b) Sample 3001B.

(c) Sample 2601C. (d) A plot showing the relationship between concordant age vs Th/U ratio of the analyzed spots.

Figure 7. Pressure-temperature diagram showing a *P-T-t* path (red arrows) for Perlebandet rocks. Evolution of microstructure for sample 3001G is given as sketches (1)-(3) and change of fluid compositions along the *P-T-t* path is also indicated. Note that Cl-rich fluid is present from prograde metamorphism. Petrogenetic grid for the NaKFMASH system with contours of Mg/(Fe+Mg) = 0.1-0.4 in garnet in divariant Als + Grt + Bt assemblage are from Spear et al. (1999). Prograde, peak and retrograde *P-T* estimates by the Grt-Bt geothermometer (GB) (Holdaway et al., 1997; Holdaway, 2000) and the GASP geobarometer (Holdaway, 2001) are shown as gray, red and black squares, respectively. Peak *P-T* estimate by the Zr-in-rutile geothermometer (Tomkins et al., 2007), the Grt-Bt geothermometer (Holdaway et al., 1997; Holdaway, 2000) and the GASP geobarometer (Holdaway, 2001) is shown by a red broken diamond. Zr-in-rutile$_{1550}$ represents a result of the Zr-in-rutile geothermometer (Tomkins et al., 2007) for 1550 ppm Zr, and Zr-in-rutile$_{2200}$ represents that for 2200 ppm Zr. Retrograde *P-T* estimates by the Grt-Bt geothermometer (Holdaway et al., 1997; Holdaway, 2000) and the GBPQ geobarometer (Wu et al., 2004) using compositions of garnet rims and biotite and plagioclase in the biotite-plagioclase intergrowths are shown as solid squares, where green, blue and brown squares are from samples 3001B, 3001G and 2601C, respectively. These

estimates would accompany errors of ±50 ºC and ±0.1 GPa, which are not shown for simplicity. Numbers of the reactions correspond to those in the text. Reactions (4)-(6) are not shown.

Figure 8. Simplified cross section showing the tectonic model for the continental collision in the SRM, modified after Osanai et al. (2013). Chlorine-rich fluid infiltration in Perlebandet presumably took place at the uppermost part of the footwall of the MBT. Chlorine-rich fluid infiltration in Balchenfjella is dated to be at ca. 603 Ma (Higashino et al., 2013), and would be an older event than that in Perlebandet (ca. 580 Ma). BDF: Balchen Detachment Fault (Ishikawa et al., 2013). [*1] This study, [*2] Higashino et al. (2015a), [*3] Higashino et al. (2013).

Table 1. Representative mineral analysis of biotite, garnet and plagioclase from samples 3001G, 3001B and 2601C. The $\log[f(H_2O)/f(HCl)]$ and $\log[f(H_2O)/f(HF)]$ values of the fluid that possibly coexisted with Cl-bearing biotite (Munoz, 1992) are also shown. [*1] Based on Munoz (1992). [*2] Temperature used in calculating $\log[f(H_2O)/f(HCl)]$ and $\log[f(H_2O)/f(HF)]$ values of the fluid possibly coexisted with biotite. Temperature was estimated using the Grt-Bt geothermometer (Holdaway et al., 1997; Holdaway, 2000) and the GASP (Holdaway, 2001) and Grt-Bt-Pl-Qtz (Wu et al., 2004) geobarometers. [*3] Temperature was estimated using Zr-in-rutile geothermometer by Tomkins et al. (2006) and GASP geobarometer (Holdaway, 2001).

Supplementary Table 2. Summary of the results of LA-ICPMS U-Pb zircon dating.

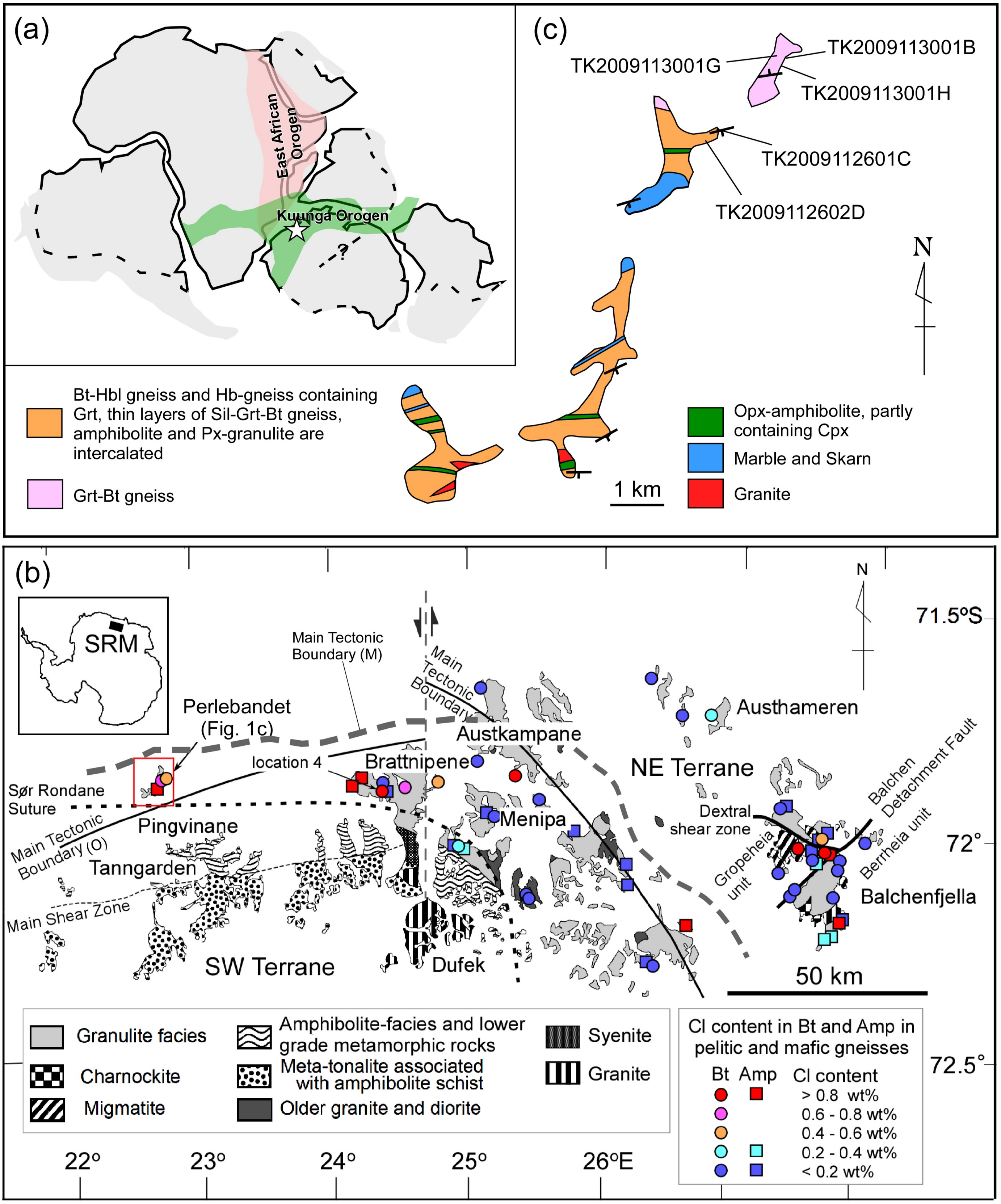

Kawakami et al. Fig. 1

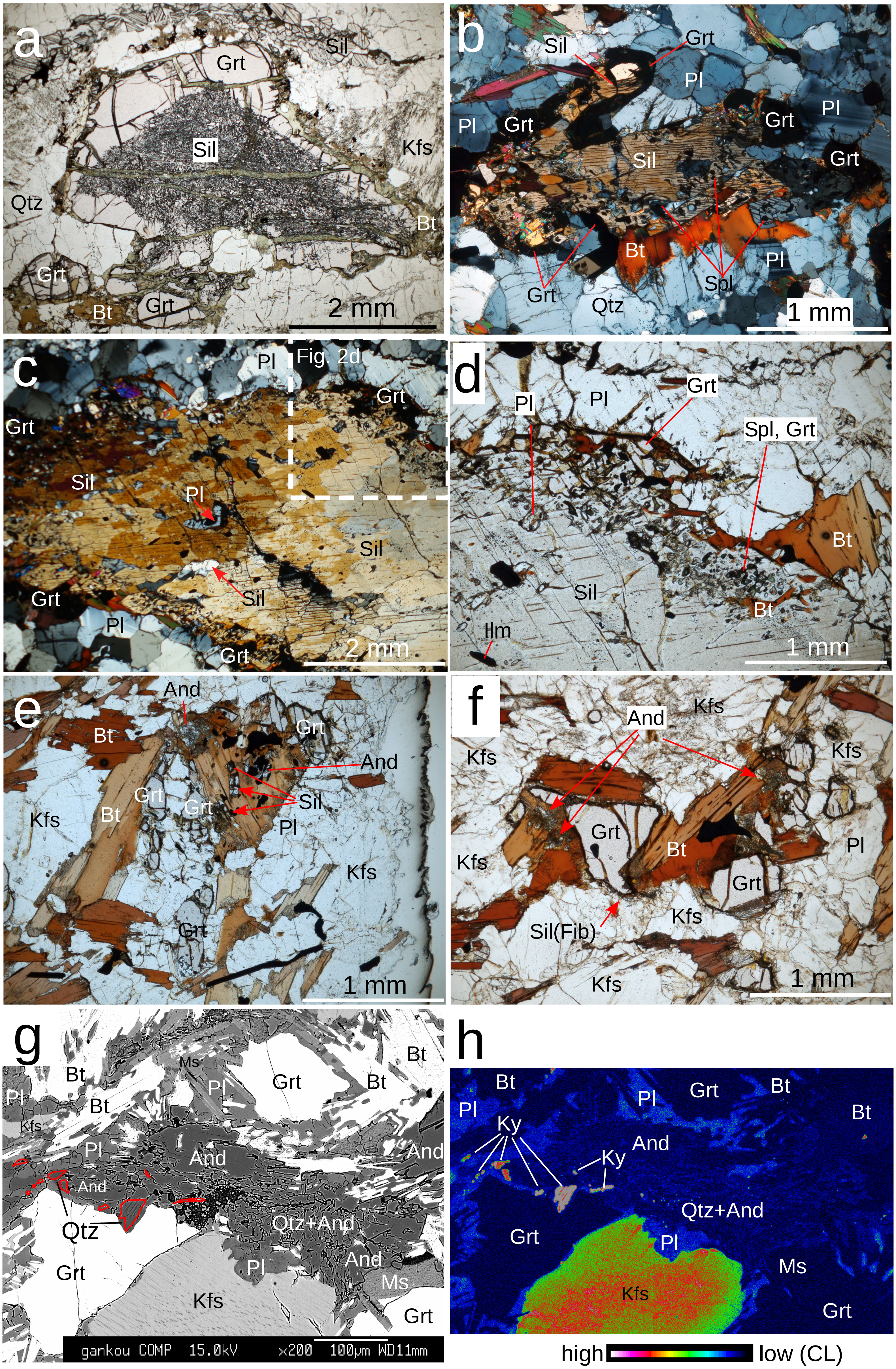

Kawakami et al. Fig. 2

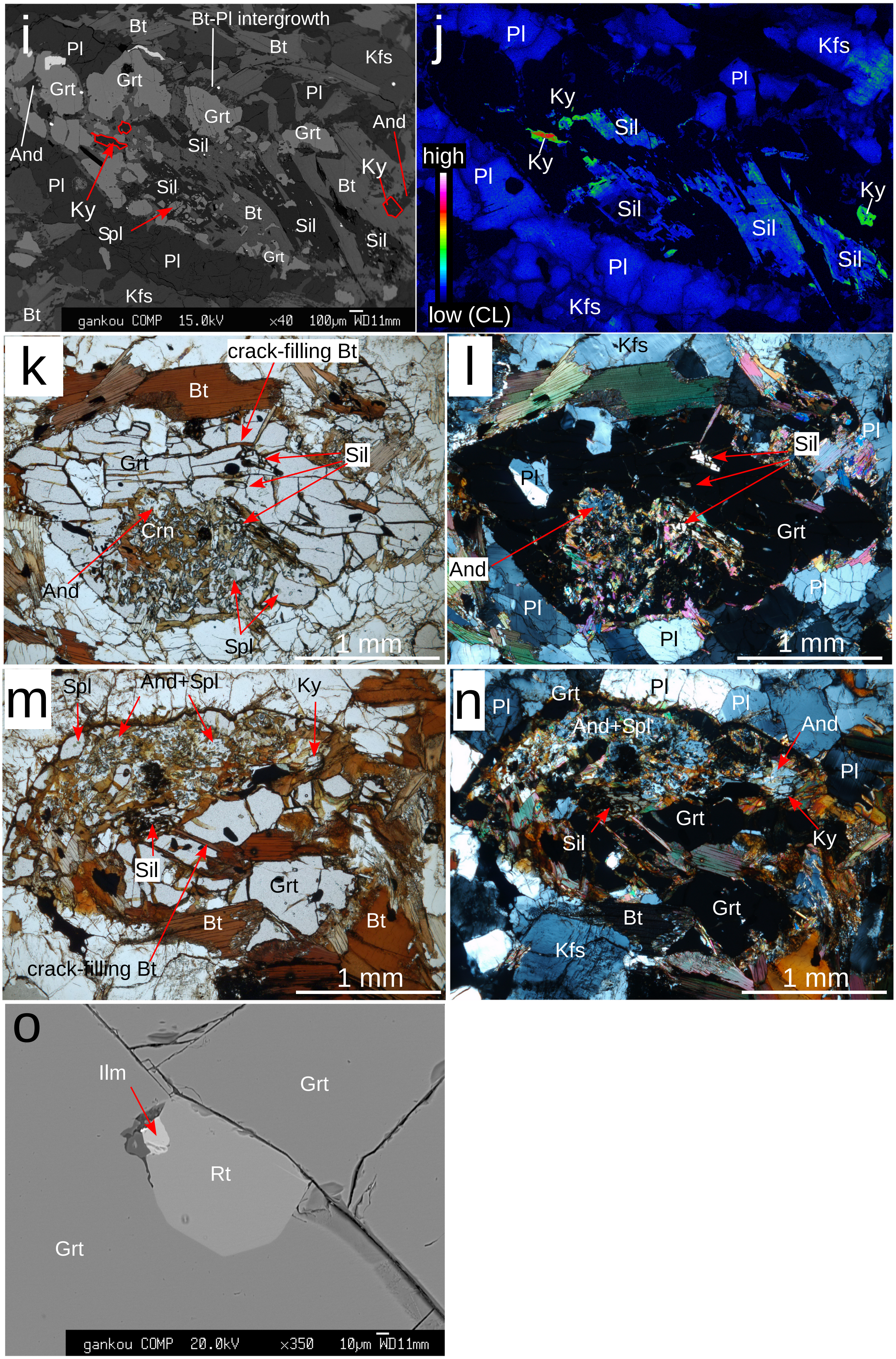

Kawakami et al Fig 2 (continued)

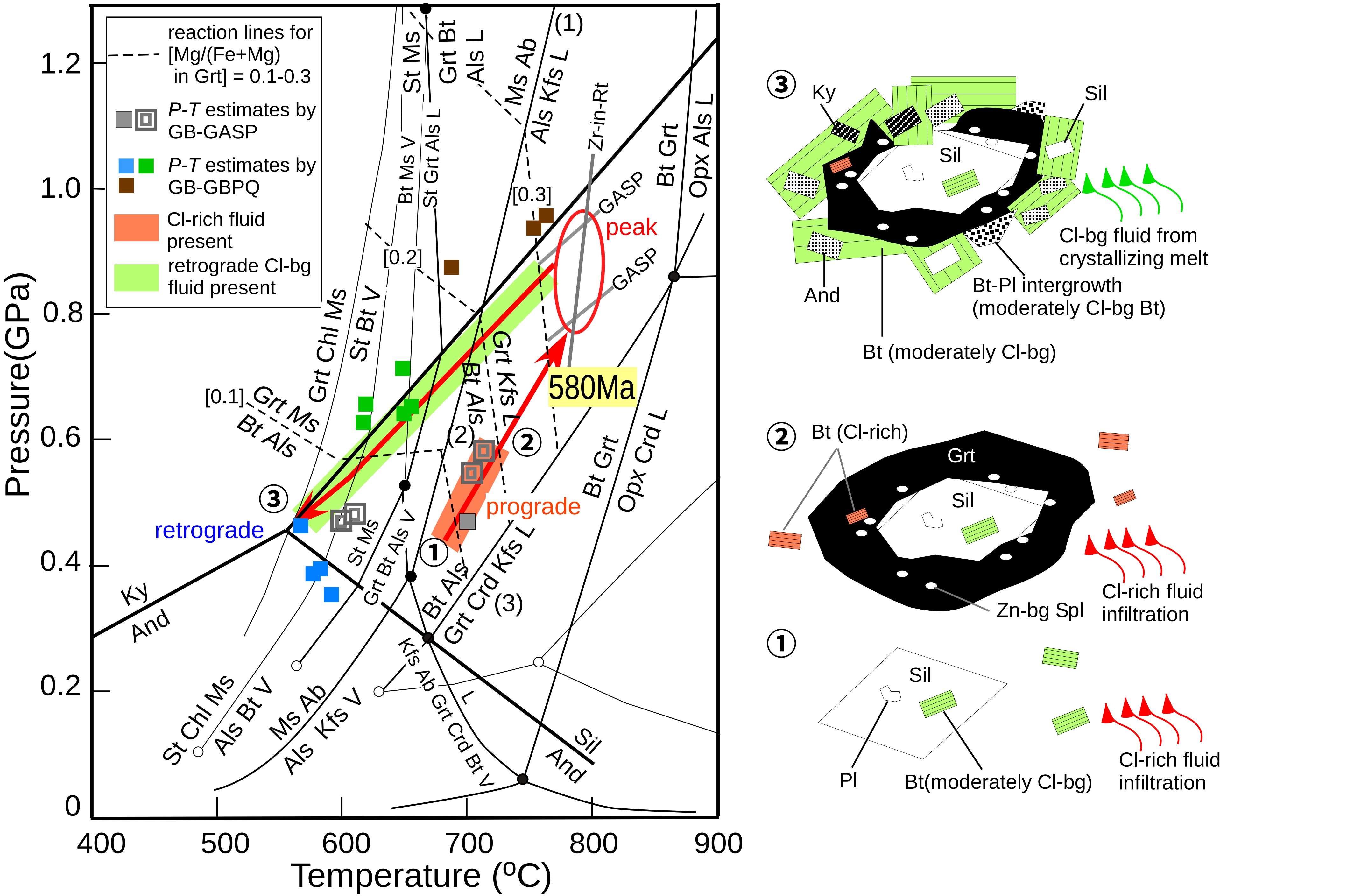

Kawakami et al. Fig 7

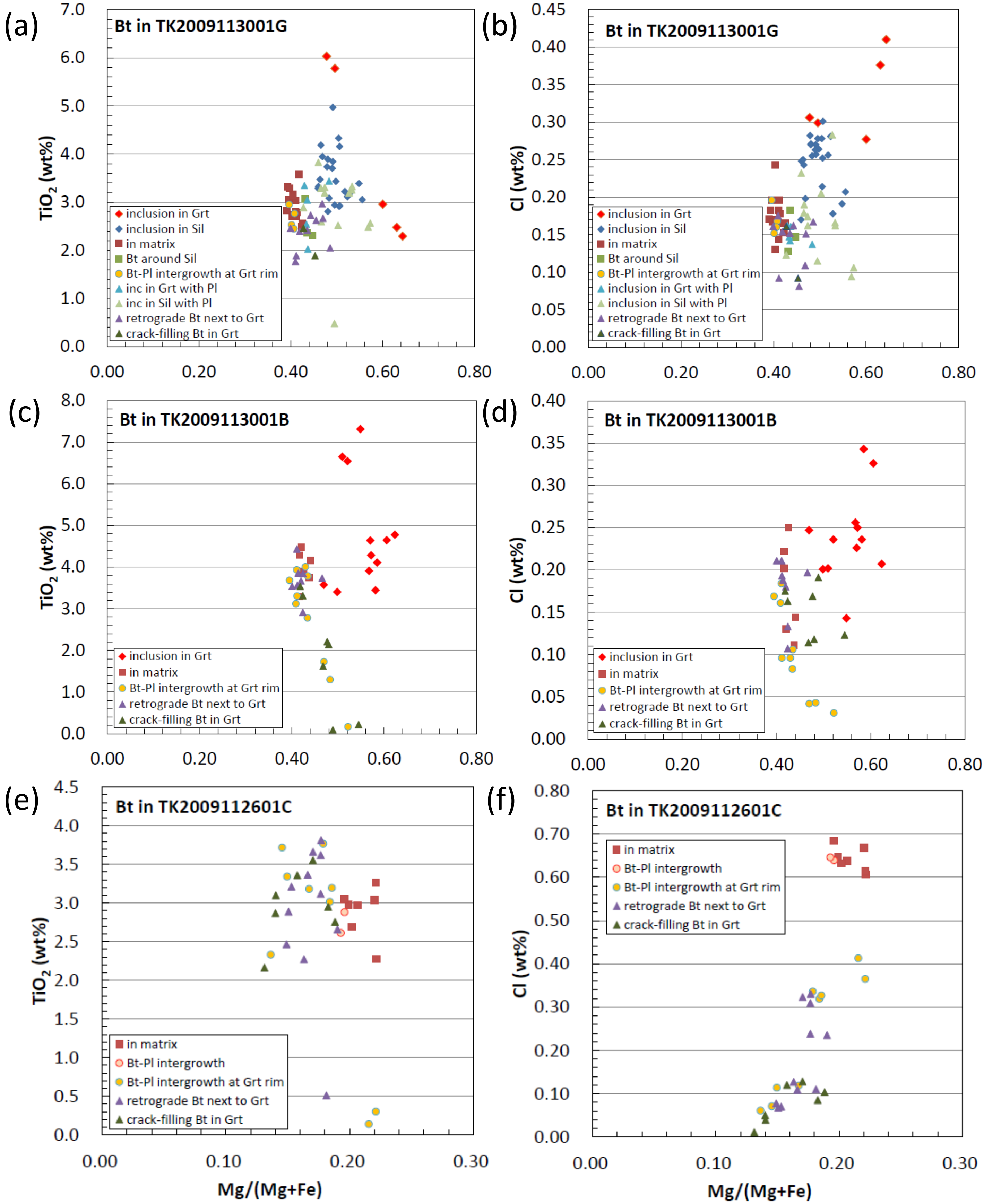

Kawakami et al. Fig. 3

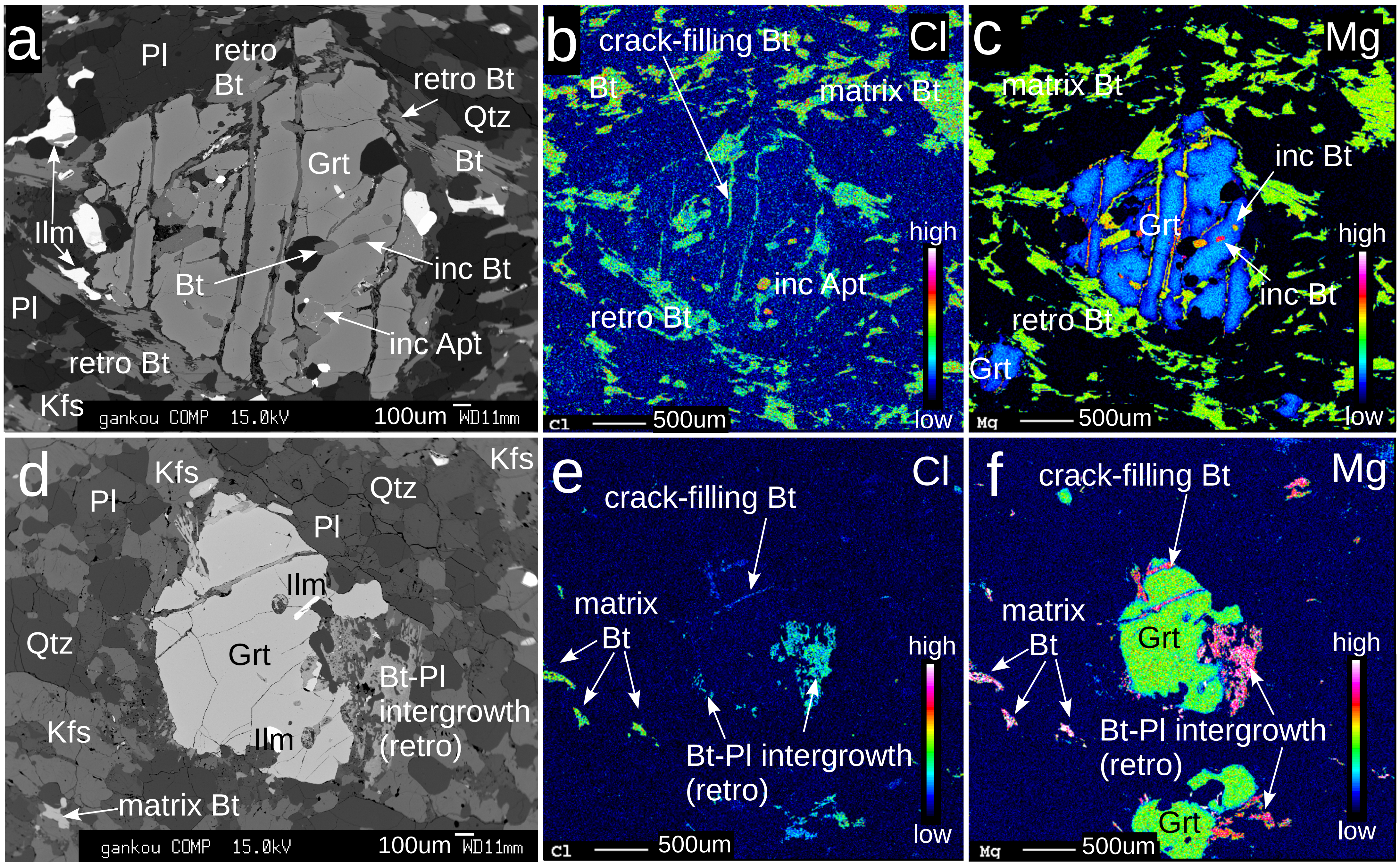

Kawakami et al Fig 4

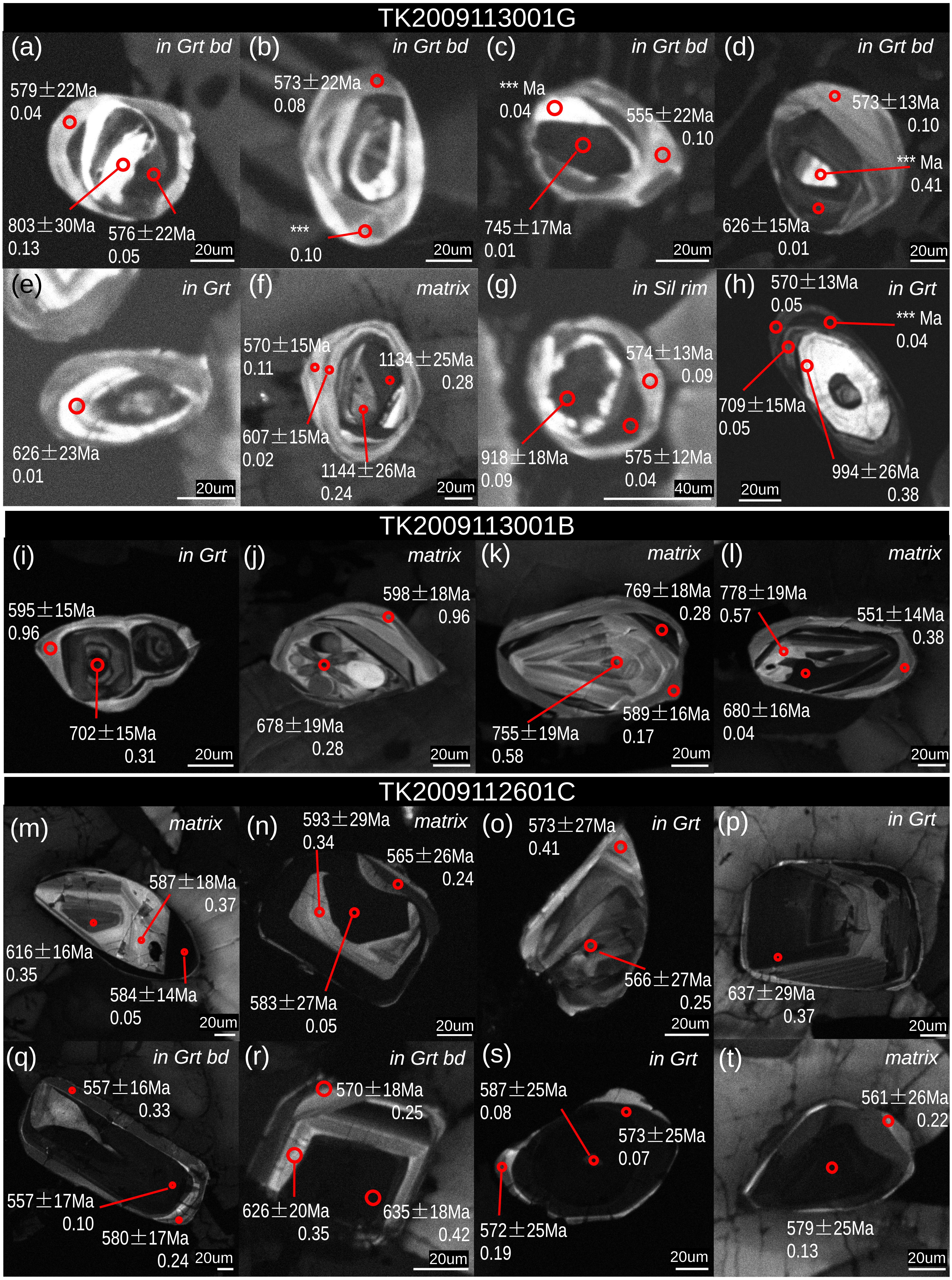

Fig. 5 Kawakami et al.

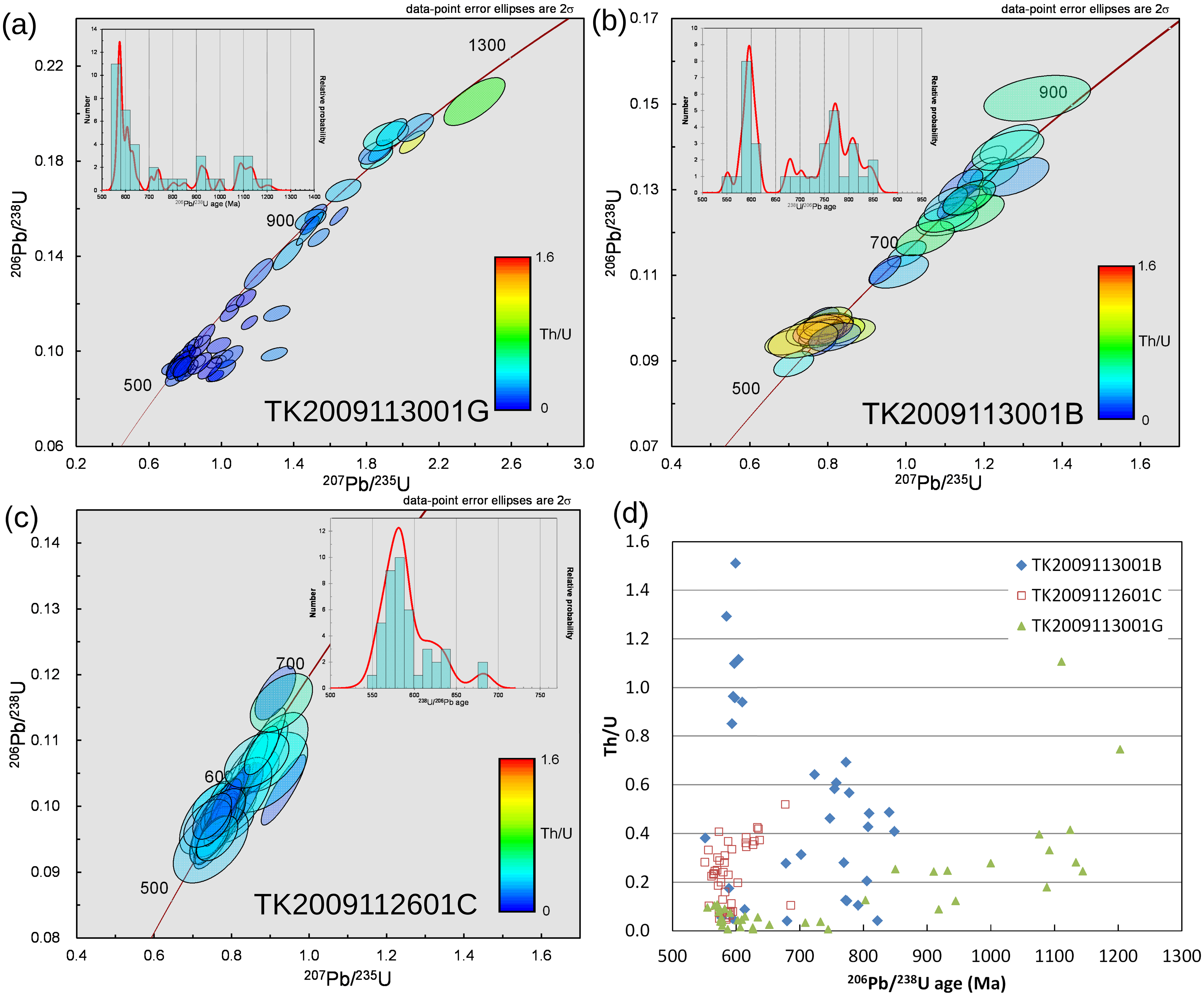

Kawakami et al. Fig. 6

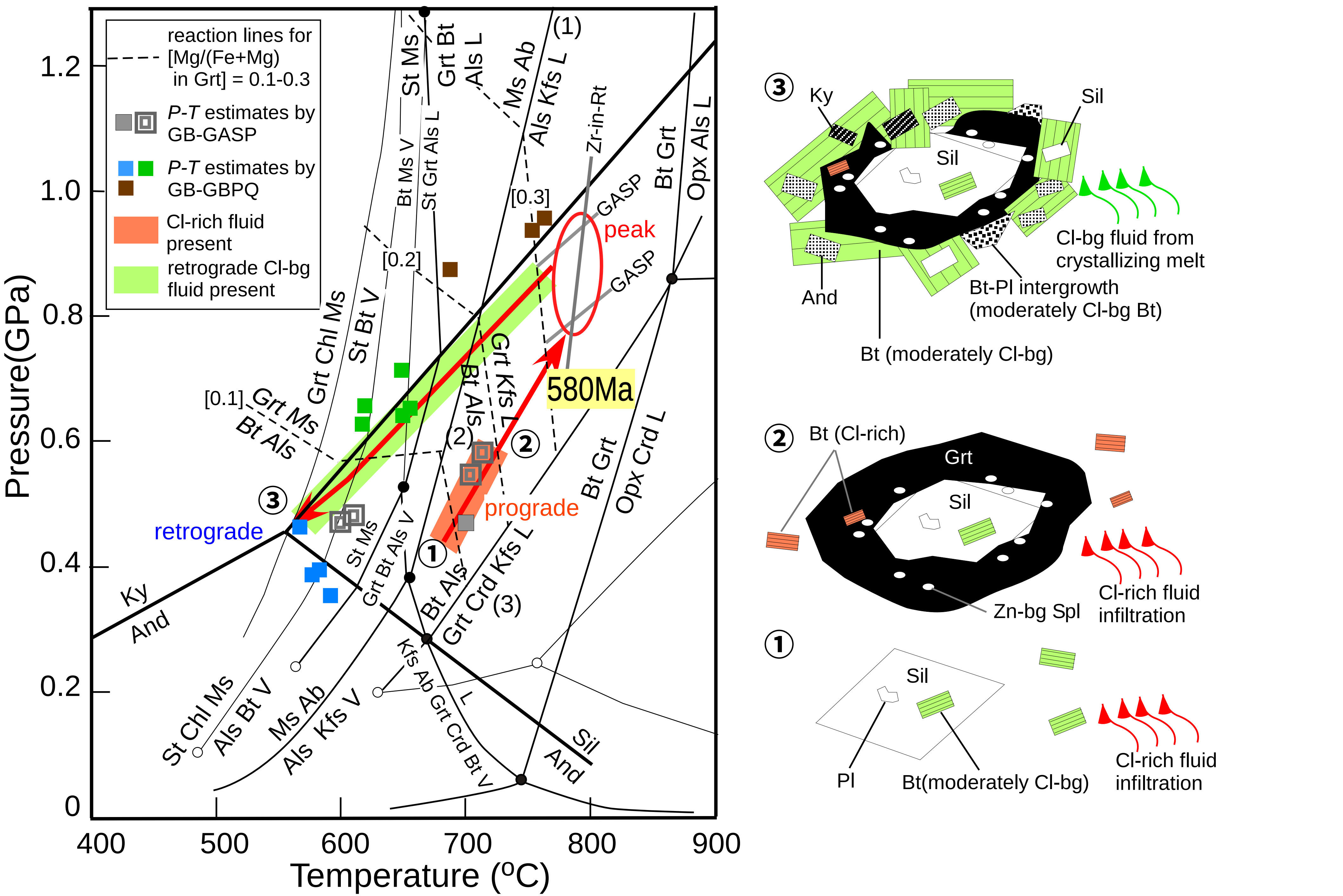

Kawakami et al. Fig 7

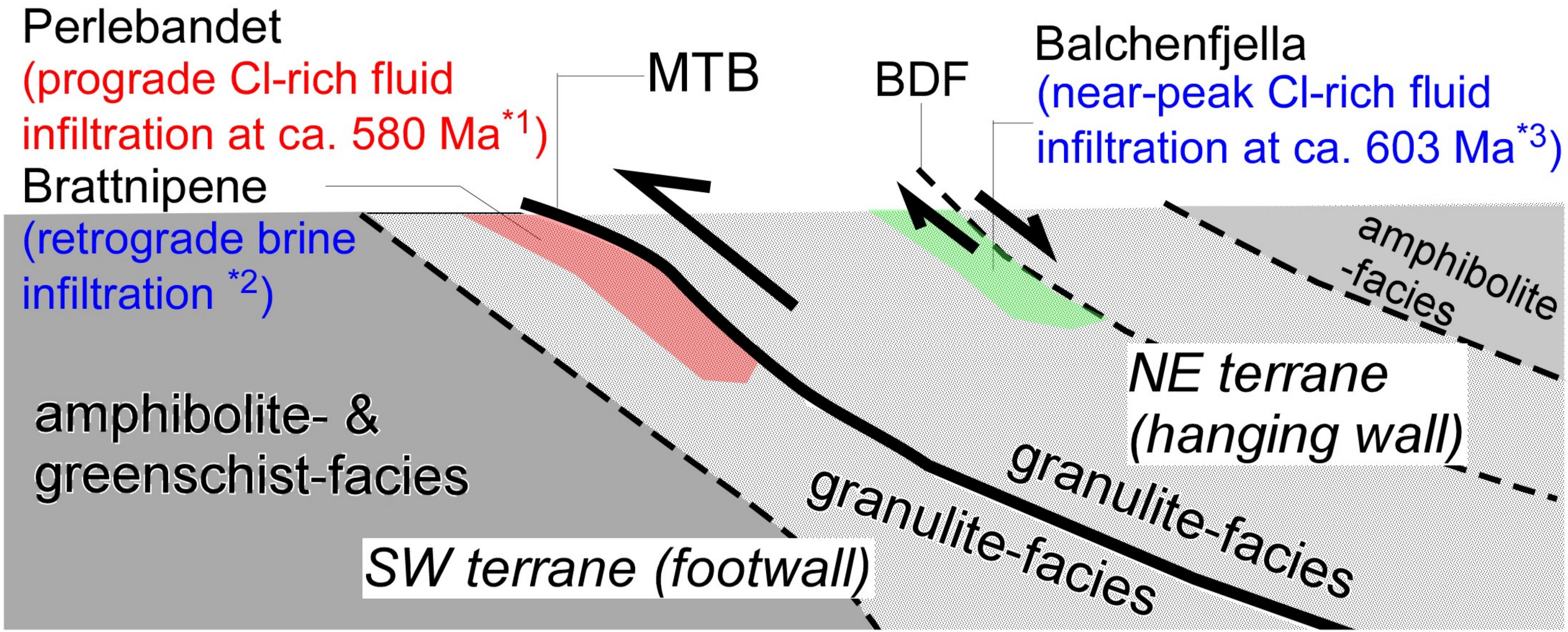

Fig. 8 Kawakami et al.

sample	TK2009113001G																TK2009112601C				
mineral	Pl	Pl	Pl	Pl	Grt	Grt	Grt	Grt	Spl	Bt	Bt	Bt	Bt	Bt	Bt	Bt	Grt	Grt	Pl	Pl	Pl
occurrence	inclusion in Sil	inclusion in Sil	Pl moat around Sil (Sil side)	Pl moat around Sil (Kfs side)	overgrowth on Sil	overgrowth on Sil	in matrix	in matrix	inclusion in Sil rim	inclusion in Grt	inclusion in Sil	in matrix (isolated)	in matrix (isolated)	Bt-Pl intergrowth replacing Grt	retrograde Bt next to Grt	crack-filling Bt in Grt	in matrix	in matrix	in matrix	in matrix	Bt-Pl intergrowth replacing Grt
core/rim	core	rim			core	rim	core	rim									rim	core	rim	core	
SiO_2	59.65	59.71	61.01	62.14	38.95	37.76	37.81	37.48	0.14	37.70	34.78	36.68	35.85	35.29	34.92	35.44	38.00	38.33	61.41	61.19	61.89
TiO_2	0.00	0.06	0.00	0.10	0.00	0.02	0.05	0.00	0.00	2.29	4.19	3.15	3.58	2.76	2.39	1.89	0.01	0.08	0.01	0.00	0.03
Al_2O_3	26.02	25.63	24.76	23.72	22.00	21.18	21.72	21.26	61.03	19.12	18.50	18.91	19.30	19.04	18.94	20.28	21.23	21.10	23.93	24.06	23.88
Cr_2O_3	0.00	0.00	0.00	0.00	0.02	0.08	0.00	0.06	0.11	0.00	0.06	0.10	0.05	0.07	0.09	0.01	0.00	0.04	0.00	0.00	0.00
FeO	0.11	0.05	0.00	0.02	32.31	36.58	35.68	36.04	27.07	13.57	19.09	20.20	20.43	20.39	21.17	18.59	33.74	31.81	0.06	0.02	0.38
ZnO	n.d.	n.d.	n.d.	n.d.	n.d.	n.d.	n.d.	n.d.	6.03	n.d.	n.d.	n.d.	n.d.	n.d.	n.d.	n.d.	n.d.	n.d.	n.d.	n.d.	n.d.
MnO	0.01	0.00	0.02	0.00	0.62	1.44	0.84	1.83	0.06	0.11	0.04	0.02	0.06	0.04	0.14	0.05	0.77	0.82	0.03	0.00	0.02
MgO	0.00	0.00	0.00	0.00	4.90	2.38	3.26	2.48	5.56	13.74	9.33	7.68	8.21	7.89	7.90	8.64	1.48	1.95	0.01	0.00	0.02
CaO	7.78	6.92	6.54	5.52	2.29	1.49	2.27	1.44	0.00	0.08	0.02	0.00	0.00	0.01	0.00	0.00	6.36	7.17	5.90	5.94	5.60
BaO	0.15	0.06	0.09	0.02	0.11	0.06	0.11	0.00	0.00	0.06	0.30	0.08	0.16	0.05	0.00	0.00	0.09	0.00	0.02	0.00	0.00
Na_2O	7.24	7.65	7.95	8.69	0.00	0.02	0.04	0.02	0.00	0.19	0.05	0.12	0.10	0.11	0.12	0.16	0.07	0.00	8.14	8.20	8.35
K_2O	0.23	0.19	0.25	0.16	0.02	0.01	0.00	0.00	0.04	9.13	9.58	9.63	9.56	10.01	9.77	9.87	0.01	0.03	0.28	0.15	0.15
F	n.d.	n.d.	n.d.	n.d.	n.d.	n.d.	n.d.	n.d.	n.d.	0.36	0.08	0.06	0.09	0.16	0.07	0.16	n.d.	n.d.	n.d.	n.d.	n.d.
Cl	n.d.	n.d.	n.d.	n.d.	n.d.	n.d.	n.d.	n.d.	n.d.	0.41	0.24	0.24	0.17	0.17	0.15	0.09	n.d.	n.d.	n.d.	n.d.	n.d.
-O≡F	n.d.	n.d.	n.d.	n.d.	n.d.	n.d.	n.d.	n.d.	n.d.	0.15	0.03	0.03	0.04	0.07	0.03	0.07	n.d.	n.d.	n.d.	n.d.	n.d.
-O≡Cl	n.d.	n.d.	n.d.	n.d.	n.d.	n.d.	n.d.	n.d.	n.d.	0.09	0.05	0.05	0.04	0.04	0.03	0.02	n.d.	n.d.	n.d.	n.d.	n.d.
Total	101.18	100.26	100.62	100.37	101.22	101.03	101.78	100.61	100.04	96.51	96.16	96.80	97.48	95.87	95.60	95.09	101.76	101.32	99.78	99.56	100.31
number of O	8	8	8	8	12	12	12	12	4	22	22	22	22	22	22	22	12	12	8	8	8
Si	2.64	2.66	2.70	2.75	3.03	3.02	2.98	3.01	0.00	5.50	5.28	5.52	5.37	5.40	5.37	5.40	3.01	3.03	2.73	2.73	2.74
Ti	0.00	0.00	0.00	0.00	0.00	0.00	0.00	0.00	0.00	0.25	0.48	0.36	0.40	0.32	0.28	0.22	0.00	0.00	0.00	0.00	0.00
Al	1.36	1.34	1.29	1.24	2.02	2.00	2.02	2.01	2.00	3.29	3.31	3.35	3.41	3.43	3.43	3.64	1.98	1.96	1.26	1.27	1.25
Cr	0.00	0.00	0.00	0.00	0.00	0.00	0.00	0.00	0.00	0.00	0.01	0.01	0.01	0.01	0.01	0.00	0.00	0.00	0.00	0.00	0.00
Fe	0.00	0.00	0.00	0.00	2.10	2.45	2.36	2.42	0.63	1.66	2.42	2.54	2.56	2.61	2.72	2.37	2.23	2.10	0.00	0.00	0.01
Mn	0.00	0.00	0.00	0.00	0.04	0.10	0.06	0.12	0.00	0.01	0.00	0.00	0.01	0.00	0.02	0.01	0.05	0.05	0.00	0.00	0.00
Mg	0.00	0.00	0.00	0.00	0.57	0.28	0.38	0.30	0.23	2.99	2.11	1.72	1.83	1.80	1.81	1.96	0.17	0.23	0.00	0.00	0.00
Ca	0.37	0.33	0.31	0.26	0.19	0.13	0.19	0.12	0.00	0.01	0.00	0.00	0.00	0.00	0.00	0.00	0.54	0.61	0.28	0.28	0.27
Ba	0.00	0.00	0.00	0.00	0.00	0.00	0.00	0.00	0.00	0.00	0.02	0.00	0.01	0.00	0.00	0.00	0.00	0.00	0.00	0.00	0.00
Zn	n.d.	n.d.	n.d.	n.d.	n.d.	n.d.	n.d.	n.d.	0.12	n.d.	n.d.	n.d.	n.d.	n.d.	n.d.	n.d.	n.d.	n.d.	n.d.	n.d.	n.d.
Na	0.62	0.66	0.68	0.74	0.00	0.00	0.01	0.00	0.00	0.05	0.02	0.03	0.03	0.03	0.04	0.05	0.01	0.00	0.70	0.71	0.72
K	0.01	0.01	0.01	0.01	0.00	0.00	0.00	0.00	0.00	1.70	1.85	1.85	1.83	1.95	1.92	1.92	0.00	0.00	0.02	0.01	0.01
F	n.d.	n.d.	n.d.	n.d.	n.d.	n.d.	n.d.	n.d.	n.d.	0.17	0.04	0.03	0.04	0.08	0.04	0.08	n.d.	n.d.	n.d.	n.d.	n.d.
Cl	n.d.	n.d.	n.d.	n.d.	n.d.	n.d.	n.d.	n.d.	n.d.	0.10	0.06	0.06	0.04	0.04	0.04	0.02	n.d.	n.d.	n.d.	n.d.	n.d.
Total cation	5.00	5.00	5.00	5.01	7.96	7.98	8.01	7.99	2.99	15.48	15.51	15.39	15.45	15.56	15.60	15.55	8.01	7.99	5.00	5.00	5.00
$Mg/(Fe_{total}+Mg)$					0.21	0.10	0.14	0.11	0.27	0.64	0.47	0.40	0.42	0.41	0.40	0.45	0.07	0.10			
An	37.0	33.0	31.0	25.7															28.2	28.3	26.8
$\log(f_{H2O}/f_{HCl})$ of fluid *1										3.65	3.94			4.24	4.28						
$\log(f_{H2O}/f_{HCl})$ of fluid *2										0.12	1.19			2.19	2.25						
$\log(f_{H2O}/f_{HF})$ of fluid *1										4.31	5.07			5.12	5.46						
Temperature (°C)										800 *4	700 *3			580 *3	580 *3						

sample	TK2009112601C						TK2009113001B											
mineral	Bt	Bt	Bt	Bt	Bt	Bt	Grt	Grt	Pl	Pl	Bt	Bt	Bt	Bt	Bt	Bt	Bt	Bt
occurrence	in matrix	in matrix	Bt-Pl intergrowth replacing Grt	Bt-Pl intergrowth replacing Grt	retrograde Bt next to Grt	crack-filling Bt in Grt	in matrix	in matrix	in matrix	Bt-Pl intergrowth replacing Grt	inclusion in Grt	inclusion in Grt	in matrix	in matrix	in matrix (near Grt)	Bt-Pl intergrowth replacing Grt	retrograde Bt next to Grt	crack-filling Bt in Grt
core/rim							core	rim	core						rim			
SiO_2	35.22	34.90	34.57	34.90	34.77	33.93	38.63	37.82	59.05	54.60	37.27	38.17	37.25	37.06	36.33	37.24	35.79	36.52
TiO_2	2.28	3.12	3.72	0.30	0.51	2.95	0.06	0.11	0.04	0.07	4.11	3.91	4.16	3.75	4.29	0.17	3.56	0.09
Al_2O_3	17.88	16.62	16.87	18.70	19.64	17.22	22.05	21.69	25.41	28.26	16.65	15.82	16.24	16.59	16.91	18.54	17.58	19.49
Cr_2O_3	0.04	0.01	0.03	0.04	0.00	0.00	0.00	0.00	0.00	0.04	0.00	0.04	0.01	0.03	0.02	0.05	0.00	0.02
FeO	27.96	31.02	31.10	28.37	27.47	29.95	32.35	33.11	0.05	0.33	15.95	17.35	20.95	21.62	22.84	19.80	22.46	21.06
ZnO	n.d.	n.d.	n.d.	n.d.	n.d.	n.d.	n.d.	n.d.	n.d.	n.d.	n.d.	n.d.	n.d.	n.d.	n.d.	n.d.	n.d.	n.d.
MnO	0.16	0.00	0.07	0.02	0.00	0.08	0.74	0.92	0.04	0.02	0.00	0.00	0.00	0.00	0.00	0.00	0.00	0.18
MgO	4.47	3.74	2.97	4.52	3.41	3.76	4.70	2.99	0.01	0.00	12.61	12.77	9.24	9.44	9.14	12.12	8.82	11.30
CaO	0.00	0.03	0.01	0.11	0.02	0.04	3.45	4.48	7.48	11.12	0.05	0.01	0.00	0.01	0.00	0.04	0.00	0.05
BaO	0.13	0.06	0.12	0.00	0.00	0.17	0.00	0.01	0.00	0.09	0.34	0.13	0.14	0.13	0.17	0.00	0.00	0.00
Na_2O	0.05	0.04	0.03	0.08	0.04	0.09	0.00	0.02	7.34	5.24	0.08	0.12	0.10	0.08	0.04	0.05	0.02	0.06
K_2O	8.19	7.49	7.92	7.51	9.53	7.20	0.00	0.00	0.19	0.14	8.07	8.12	8.27	8.12	7.88	8.18	8.16	8.23
F	0.06	0.00	0.00	0.18	0.00	0.00	n.d.	n.d.	n.d.	n.d.	0.20	0.30	0.08	0.04	0.00	0.12	0.00	0.10
Cl	0.61	0.24	0.07	0.37	0.11	0.09	n.d.	n.d.	n.d.	n.d.	0.34	0.26	0.14	0.11	0.22	0.03	0.19	0.19
-O≡F	0.03	0.00	0.00	0.08	0.00	0.00	n.d.	n.d.	n.d.	n.d.	0.09	0.13	0.03	0.02	0.00	0.05	0.00	0.04
-O≡Cl	0.14	0.05	0.02	0.08	0.02	0.02	n.d.	n.d.	n.d.	n.d.	0.08	0.06	0.03	0.03	0.05	0.01	0.04	0.04
Total	96.87	97.22	97.45	94.94	95.47	95.46	101.98	101.14	99.62	99.91	95.52	96.79	96.50	96.93	97.77	96.28	96.54	97.20
number of O	22	22	22	22	22	22	12	12	8	8	22	22	22	22	22	22	22	22
Si	5.49	5.47	5.42	5.53	5.49	5.40	3.00	2.99	2.65	2.47	5.55	5.63	5.61	5.56	5.44	5.55	5.42	5.44
Ti	0.27	0.37	0.44	0.04	0.06	0.35	0.00	0.01	0.00	0.00	0.46	0.43	0.47	0.42	0.48	0.02	0.41	0.01
Al	3.29	3.07	3.12	3.49	3.66	3.23	2.02	2.02	1.34	1.51	2.92	2.75	2.88	2.93	2.99	3.26	3.14	3.42
Cr	0.01	0.00	0.00	0.01	0.00	0.00	0.00	0.00	0.00	0.00	0.00	0.01	0.00	0.00	0.00	0.01	0.00	0.00
Fe	3.65	4.07	4.08	3.76	3.63	3.99	2.10	2.19	0.00	0.01	1.99	2.14	2.64	2.71	2.86	2.47	2.85	2.62
Mn	0.02	0.00	0.01	0.00	0.00	0.01	0.05	0.06	0.00	0.00	0.00	0.00	0.00	0.00	0.00	0.00	0.00	0.02
Mg	1.04	0.87	0.69	1.07	0.80	0.89	0.54	0.35	0.00	0.00	2.80	2.81	2.07	2.11	2.04	2.69	1.99	2.51
Ca	0.00	0.00	0.00	0.02	0.00	0.01	0.29	0.38	0.36	0.54	0.01	0.00	0.00	0.00	0.00	0.01	0.00	0.01
Ba	0.01	0.00	0.01	0.00	0.00	0.01	0.00	0.00	0.00	0.00	0.02	0.01	0.01	0.01	0.01	0.00	0.00	0.00
Zn	n.d.	n.d.	n.d.	n.d.	n.d.	n.d.	n.d.	n.d.	n.d.	n.d.	n.d.	n.d.	n.d.	n.d.	n.d.	n.d.	n.d.	n.d.
Na	0.01	0.01	0.01	0.02	0.01	0.03	0.00	0.00	0.64	0.46	0.02	0.03	0.03	0.02	0.01	0.01	0.01	0.02
K	1.63	1.50	1.59	1.52	1.92	1.46	0.00	0.00	0.01	0.01	1.53	1.53	1.59	1.55	1.51	1.56	1.58	1.56
F	0.03	0.00	0.00	0.09	0.00	0.00	n.d.	n.d.	n.d.	n.d.	0.10	0.14	0.04	0.02	0.00	0.06	0.00	0.05
Cl	0.16	0.06	0.02	0.10	0.03	0.02	n.d.	n.d.	n.d.	n.d.	0.09	0.06	0.04	0.03	0.06	0.01	0.05	0.05
Total cation	15.41	15.38	15.37	15.46	15.58	15.38	7.99	8.00	5.00	5.01	15.31	15.34	15.29	15.33	15.34	15.58	15.39	15.63
$Mg/(Fe_{total}+Mg)$	0.22	0.18	0.15	0.22	0.18	0.18	0.21	0.14			0.59	0.57	0.44	0.44	0.42	0.52	0.41	0.49
An									35.6	53.6								
$\log(f_{H2O}/f_{HCl})$ of fluid *1			4.19	3.50	4.02						3.70	3.82				4.95	4.09	
$\log(f_{H2O}/f_{HCl})$ of fluid *2			2.02	1.14	1.76						0.31	0.47				2.32	1.74	
$\log(f_{H2O}/f_{HF})$ of fluid *1			–	4.26	–						4.52	4.33				5.17	–	
Temperature (°C)			760 *3	760 *3	760 *3						800 *4	800 *4				640 *3	640 *3	

	occurrence	zoning	$^{207}Pb/^{235}U$	error (± 2S.D.)	$^{206}Pb/^{238}U$	error (± 2S.D.)	Error correlation	$^{207}Pb/^{206}Pb$	error (± 2S.D.)	$^{207}Pb/^{235}U$ age (Ma)	error (± 2S.D., Ma)	$^{206}Pb/^{238}U$ age (Ma)	error (± 2S.D., Ma)	$^{207}Pb/^{206}Pb$ age (Ma)	error (± 2S.D., Ma)	Concordance (%)	Th/U	U (ppm)	error (± 2S.D., ppm)	Th (ppm)	error (± 2S.D., ppm)	Pb (ppm)	error (± 2S.D., ppm)
TK2009112601-51A	inc in garnet	core	0.788945	0.039112	0.095355	0.004257	0.901	0.060007	0.001293	591	22	587	25	604	47	101	0.08	3121	448	234	67	375	304
TK2009112601-51B	inc in garnet	rim	0.762783	0.05415	0.092749	0.004298	0.653	0.059647	0.003208	576	32	572	25	591	121	101	0.19	322	46	60	17	39	32
TK2009112601-51C	inc in garnet	mantle	0.782543	0.040865	0.092992	0.004169	0.859	0.061032	0.001634	587	24	573	25	640	59	102	0.07	1624	233	121	35	190	155
TK2009112601-53A	in matrix	core	0.755302	0.038372	0.093941	0.004201	0.880	0.058313	0.001405	571	22	579	25	542	54	99	0.13	2270	326	292	84	272	221
TK2009112601-53B	in matrix	rim	0.751175	0.048011	0.090952	0.004444	0.764	0.0599	0.002468	569	28	561	26	600	92	101	0.22	633	69	142	31	76	57
TK2009112601-55A	in matrix	core	0.87678	0.050424	0.102448	0.004635	0.787	0.06207	0.002204	639	28	629	27	677	78	102	0.37	710	102	261	75	99	80
TK2009112601-55B	in matrix	mantle	0.900365	0.074135	0.103273	0.004918	0.578	0.063231	0.004247	652	40	634	29	716	150	103	0.42	171	25	73	21	24	20
TK2009112601-55C	in matrix	rim	0.815548	0.047895	0.09628	0.004364	0.772	0.061435	0.002294	606	27	593	26	654	82	102	0.11	678	97	76	22	84	68
TK2009112601-56A	inc in garnet	rim	0.727565	0.058196	0.093144	0.004386	0.589	0.056652	0.003663	555	35	574	26	478	150	97	0.29	228	33	66	19	28	23
TK2009112601-56B	inc in garnet	mantle	0.818644	0.042554	0.097995	0.004392	0.862	0.060589	0.001596	607	24	603	26	625	58	101	0.20	1624	233	321	92	208	169
TK2009112601-57A	inc in garnet	core	0.766414	0.042563	0.09441	0.004254	0.811	0.058877	0.001911	578	25	582	25	563	72	99	0.28	1005	144	282	81	126	102
TK2009112601-57B	inc in garnet	rim	0.742705	0.04776	0.091452	0.004183	0.711	0.058901	0.002662	564	28	564	25	563	102	100	0.23	482	69	112	32	58	47
TK2009112601-61A	in matrix	rim	0.790243	0.048438	0.092562	0.002552	0.450	0.061919	0.00339	591	28	571	15	671	122	104	0.30	279	18	84	11	36	24
TK2009112601-61B	in matrix	rim	0.927303	0.047488	0.09752	0.004369	0.875	0.068964	0.001711	666	25	600	26	898	52	111	0.10	1714	246	167	48	218	177
TK2009112601-61C	in matrix	core	0.881331	0.088621	0.100217	0.004993	0.495	0.063781	0.005571	642	49	616	29	734	197	104	0.38	101	15	39	11	14	11
TK2009112601-62A	in matrix	rim	0.799504	0.026226	0.094873	0.002312	0.743	0.061119	0.001342	597	15	584	14	643	48	102	0.05	2506	165	118	16	311	211
TK2009112601-62B	in matrix	mantle	0.773234	0.06798	0.095387	0.002997	0.357	0.058792	0.004827	582	40	587	18	559	190	99	0.37	122	8	45	6	16	11
TK2009112601-62C	in matrix	core	0.858849	0.046529	0.100255	0.002672	0.492	0.062131	0.002931	629	26	616	16	679	104	102	0.35	353	23	122	16	52	35
TK2009112601-63A	in matrix	rim	0.763853	0.027361	0.09456	0.002327	0.687	0.058587	0.001525	576	16	582	14	552	58	99	0.16	1605	106	256	34	204	138
TK2009112601-63B	in matrix	core	0.765639	0.033241	0.095455	0.002416	0.583	0.058173	0.002052	577	19	588	14	536	79	98	0.23	755	50	174	23	98	67
TK2009112601-65	inc in garnet	mantle	0.799718	0.041597	0.096685	0.004641	0.923	0.05999	0.001201	597	24	595	27	603	44	100	0.08	4058	444	321	70	501	377
TK2009112601-66	inc in garnet	core	0.828164	0.047665	0.10013	0.004845	0.841	0.059986	0.001869	613	27	615	28	603	69	100	0.36	1100	120	397	87	151	113
TK2009112601-67	inc in garnet	core	0.804444	0.042348	0.096049	0.004615	0.913	0.060744	0.001306	599	24	591	27	630	47	101	0.08	3161	346	241	53	388	292
TK2009112601-68A	inc in garnet	core	0.747001	0.052567	0.091847	0.004535	0.702	0.058987	0.002958	566	31	566	27	567	113	100	0.25	413	45	102	22	51	38
TK2009112601-68B	inc in garnet	rim	0.757836	0.05665	0.092957	0.004625	0.666	0.059128	0.003299	573	33	573	27	572	126	100	0.41	324	36	132	29	42	32
TK2009112601-69	in matrix	mantle	0.873261	0.048714	0.103873	0.005014	0.865	0.060973	0.001705	637	27	637	29	638	61	100	0.37	1371	150	511	112	196	148
TK2009112601-70A	inc in garnet	mantle	0.772304	0.041242	0.094678	0.004553	0.901	0.059161	0.001373	581	24	583	27	573	51	100	0.05	2593	284	140	31	311	234
TK2009112601-70B	inc in garnet	core	0.809203	0.071248	0.096415	0.004928	0.581	0.060871	0.004364	602	41	593	29	635	162	101	0.33	180	20	60	13	24	18
TK2009112601-70C	inc in garnet	rim	0.751315	0.044851	0.09158	0.004445	0.813	0.0595	0.002068	569	26	565	26	585	77	101	0.24	933	102	220	48	114	86
TK2009112601-71A	in garnet b.d.	mantle	0.737393	0.079685	0.089201	0.004756	0.493	0.059955	0.005635	561	48	551	28	602	218	102	0.28	113	12	32	7	14	11
TK2009112601-71B	in garnet b.d.	core	0.772689	0.042369	0.094535	0.004556	0.879	0.05928	0.001551	581	25	582	27	577	58	100	0.31	1846	202	570	125	236	177
TK2009112601-73	inc in garnet	core	0.789002	0.041562	0.095802	0.004603	0.912	0.059731	0.00129	591	24	590	27	594	47	100	0.08	3179	348	258	56	390	293
TK2009112601-74	in matrix	mantle	0.764374	0.033423	0.09309	0.002748	0.675	0.059552	0.001921	577	19	574	16	587	72	100	0.05	2454	231	124	23	297	206
TK2009112601-75A	in matrix	mantle	0.743313	0.035873	0.090293	0.002703	0.620	0.059706	0.00226	564	21	557	16	593	84	101	0.10	1253	118	129	24	149	103
TK2009112601-75B	in matrix	rim	0.769999	0.047878	0.094104	0.002958	0.505	0.059345	0.003184	580	28	580	17	580	121	100	0.24	423	40	102	19	54	38
TK2009112601-75C	in matrix	rim	0.754307	0.043921	0.090164	0.002796	0.533	0.060675	0.00299	571	26	557	17	628	110	103	0.33	542	51	180	34	68	47
TK2009112601-76A	inc in garnet	core	0.905963	0.043657	0.112273	0.00336	0.621	0.058524	0.00221	655	24	686	20	549	85	95	0.10	1035	97	108	20	153	106
TK2009112601-76B	inc in garnet	rim	0.777846	0.032673	0.095762	0.002812	0.699	0.058911	0.001769	584	19	590	17	564	67	99	0.06	3758	354	240	45	469	325
TK2009112601-77A	in matrix	rim	0.729311	0.05081	0.092435	0.002981	0.463	0.057224	0.003534	556	30	570	18	500	142	98	0.25	314	30	78	15	40	28
TK2009112601-77B	in matrix	mantle	0.857035	0.068791	0.102049	0.00346	0.422	0.06091	0.004431	629	38	626	20	636	165	100	0.35	183	17	65	12	27	18
TK2009112601-77C	in matrix	core	0.869925	0.036949	0.103534	0.003046	0.693	0.060939	0.001867	636	20	635	18	637	67	100	0.42	2933	276	1228	231	432	300
TK2009112601-78A	in matrix	core	0.921466	0.066634	0.11078	0.003632	0.453	0.060328	0.003888	663	36	677	21	615	146	98	0.52	225	21	117	22	36	25
TK2009112601-78B	in matrix	mantle	1.462504	0.059643	0.123014	0.003608	0.719	0.086227	0.002443	915	25	748	21	1343	56	122	0.10	3424	322	355	67	588	408
TK2009112601-78C	in matrix	rim	0.741325	0.041328	0.093509	0.002867	0.550	0.057498	0.002677	563	24	576	17	511	106	98	0.20	645	61	129	24	81	56
TK2009113001B-11A	in matrix	core	1.33761	0.11176	0.151423	0.004379	0.346	0.064067	0.005022	862	50	909	25	744	175	94.9	0.54	93	12	50	13	21	14
TK2009113001B-11B	in matrix	rim	0.778667	0.035572	0.093726	0.002105	0.492	0.060254	0.002397	585	21	578	12	613	88	101	0.05	773	96	41	10	96	62
TK2009113001B-12A	inc in garnet	rim	0.794271	0.059338	0.098115	0.002616	0.357	0.058713	0.004097	594	34	603	15	556	160	98	1.12	199	25	223	55	33	21
TK2009113001B-12B	inc in garnet	mantle	0.813669	0.029937	0.096636	0.002074	0.583	0.061067	0.001825	605	17	595	12	642	66	102	0.05	1786	222	90	22	230	148
TK2009113001B-12C	inc in garnet	core	1.106515	0.065009	0.122958	0.003017	0.418	0.065268	0.003484	756	32	748	17	783	116	101	0.46	263	33	122	30	48	31
TK2009113001B-17D	inc in garnet	rim	0.737288	0.073081	0.09493	0.00345	0.367	0.056329	0.005194	561	44	585	20	465	218	95.9	1.29	125	12	161	30	20	14
TK2009113001B-21A	inc in biotite	mantle	1.227391	0.050707	0.133708	0.002953	0.535	0.066577	0.002325	813	23	809	17	825	75	101	0.48	714	89	344	85	141	91
TK2009113001B-21B	inc in biotite	core	1.158487	0.050569	0.127369	0.002849	0.512	0.065967	0.002473	781	24	773	16	805	81	101	0.69	615	76	426	106	121	78
TK2009113001B-21C	inc in biotite	rim	0.700768	0.050331	0.094408	0.002437	0.359	0.053835	0.003608	539	31	582	14	364	159	92.7	1.01	246	31	247	61	38	25
TK2009113001B-22A	in matrix	rim	0.811972	0.068571	0.097048	0.002769	0.338	0.060681	0.004823	604	39	597	16	628	181	101	1.10	148	18	162	40	25	16
TK2009113001B-22B	in matrix	mantle	0.786791	0.035351	0.099857	0.002227	0.496	0.057145	0.002229	589	20	614	13	497	88	96.1	0.09	804	100	71	18	108	70
TK2009113001B-23A	inc in garnet	rim	0.846684	0.062113	0.096741	0.002593	0.365	0.063476	0.004335	623	35	595	15	724	152	104.6	0.96	197	24	190	47	31	20
TK2009113001B-23B	inc in garnet	core	1.003796	0.040556	0.115087	0.002521	0.542	0.063258	0.002148	706	21	702	15	717	74	101	0.31	947	118	297	74	155	100
TK2009113001B-27A	in matrix	rim	1.153538	0.045532	0.12762	0.002787	0.553	0.065556	0.002156	779	22	774	16	792	71	101	0.12	913	113	112	28	159	102
TK2009113001B-27B	in matrix	core	1.282152	0.070143	0.133094	0.003718	0.511	0.069868	0.003286	838	32	805	21	924	100	104.0	0.20	277	31	57	13	51	31
TK2009113001B-27C	in matrix	mantle	1.202825	0.04595	0.136023	0.00352	0.677	0.064134	0.001802	802	21	822	20	746	61	97.5	0.04	1225	137	51	12	221	133
TK2009113001B-2A	in matrix	core	1.108003	0.061442	0.124212	0.003348	0.486	0.064696	0.003135	757	30	755	19	764	106	100	0.58	259	17	151	20	48	32
TK2009113001B-2B	in matrix	rim	0.818233	0.054712	0.095602	0.002713	0.424	0.062074	0.003758	607	31	589	16	677	135	103.1	0.17	218	14	38	5	28	19
TK2009113001B-2C	in matrix	mantle	1.103481	0.045407	0.126742	0.003193	0.612	0.063146	0.002054	755	22	769	18	713	71	98	0.28	637	42	179	24	112	76
TK2009113001B-3A	in matrix	rim	0.71351	0.041963	0.089294	0.002416	0.460	0.057953	0.003026	547	25	551	14	528	119	99	0.38	340	22	130	17	43	29
TK2009113001B-3B	in matrix	mantle	0.947184	0.033726	0.11128	0.00274	0.692	0.061733	0.001588	677	18	680	16	665	56	99	0.04	1342	89	54	7	195	132
TK2009113001B-3C	in matrix	core	1.163294	0.055279	0.12822	0.00333	0.547	0.065801	0.002618	784	26	778	19	800	86	101	0.57	381	25	216	29	72	49
TK2009113001B-4A	in matrix	core	1.266264	0.061775	0.14071	0.003806	0.555	0.065268	0.00265	831	28	849	22	783	88	98	0.41	399	45	163	37	81	48
TK2009113001B-4B	in matrix	rim	0.788545	0.063174	0.097342	0.003019	0.387	0.058752	0.00434	590	37	599	18	558	170	99	1.51	163	18	246	55	29	17
TK2009113001B-5A	in matrix	mantle	1.050245	0.061287	0.118741	0.00335	0.483	0.064149	0.003277	729	31	723	19	747	112	101	0.64	277	31	178	40	50	30
TK2009113001B-5B	in matrix	core	1.262501	0.075225	0.139266	0.003844	0.463	0.065749	0.003472	829	34	841	22	798	115	99	0.49	189	13	92	12	39	26
TK2009113001B-7A	in matrix	rim	0.784725	0.047907	0.096393	0.00273	0.464	0.059043	0.003193	588	28	593	16	569	122	99	0.85	324	36	276	62	50	30
TK2009113001B-7B	in matrix	core	1.136167	0.044608	0.12721	0.003305	0.662	0.064777	0.001907	771	21	772	19	767	63	100	0.13	1108	124	140	31	191	115
TK2009113001B-7C	in matrix	rim	0.80033	0.050941	0.09914	0.00284	0.450	0.058549	0.003328	597	29	609	17	550	129	98	0.94	284	32	267	60	45	27
TK2009113001B-8A	in matrix	rim	0.767331	0.060032	0.09714	0.002974	0.391	0.05729	0.004125	578	35	598	17	503	167	96.8	0.96	176	20	169	38	28	17
TK2009113001B-8B	in matrix	core	0.983365	0.061772	0.110959	0.003198	0.459	0.064276	0.003588	695	32	678	19	751	123	102.5	0.28	242	27	67	15	38	23
TK2009113001B-9A	in matrix	core	1.171108	0.066864	0.124656	0.003515	0.494	0.068137	0.003383	787	32	757	20	873	106	103.9	0.61	267	30	162	36	51	30
TK2009113001B-9B	in matrix	mantle	1.187953	0.044968	0.133414	0.003448	0.683	0.06458	0.001786	795	21	807	20	761	59	98	0.43	1314	147	562	126	255	153
TK2009113001B-9C	in matrix	rim	1.141784	0.046374	0.130672	0.003411	0.643	0.063372	0.001972	773	22	792	19	721	67	97.7	0.11	922	103	97	22	162	97
TK20113001G 10-1	inc in garnet	rim	0.899376	0.051048	0.099993	0.004146	0.730	0.065233	0.002529	651	28	614	24	782	84	106	0.06	567	82	33	5	57	9
TK20113001G 10-2	inc in garnet	rim	1.022433	0.045106	0.094269	0.003822	0.919	0.078662	0.001368	715	23	581	23	1164	35	123	0.02	2706	390	52	8	262	40
TK20113001G 10-3	inc in garnet	mantle	1.053029	0.039198	0.112614	0.002590	0.618	0.067818	0.001985	730	20	688	15	863	62	106	0.05	493	143	23	5	54	15
TK20113001G 1-1	inc in garnet	rim	0.865671	0.039148	0.103290	0.002303	0.493	0.060785	0.002391	633	22	634	13	632	87	100	0.01	1202	155	13	2	119	16
TK20113001G 1-2	inc in garnet	rim	0.873669	0.040272	0.101982	0.002286	0.486	0.062133	0.002503	638	22	626	13	679	88	102	0.01	1064	137	11	1	104	14
TK20113001G 2-1	inc in garnet	mantle	0.886832	0.044025	0.102939	0.004207	0.823	0.062483	0.001760	645	24	632	25	691	61	102	0.00	1105	159	4	1	111	17
TK20113001G 2-2	inc in garnet	core	0.908821	0.046630	0.106331	0.004359	0.799	0.061989	0.001913	656	25	651	25	674	67	101	0.00	893	129	1	0	93	14
TK20113001G 2-4	inc in garnet	rim	0.968519	0.035503	0.094355	0.002173	0.628	0.074446	0.002123	688	18	581	13	1054	59	118	0.07	569	165	42	9	54	15
TK20113001G 2-5	inc in garnet	rim	0.865268	0.031424	0.095150	0.001956	0.566	0.065954	0.001975	633	17	586	12	805	64	108	0.07	523	61	38	4	49	6
TK20113001G 7-1	inc in garnet	rim	0.740215	0.027448	0.092413	0.002109	0.615	0.058093	0.001698	563	16	570	12	533	65	99	0.05	697	202	35	7	62	17
TK20113001G 7-2	inc in garnet	mantle	1.010486	0.033706	0.116285	0.002624	0.676	0.063024	0.001548	709	17	709	15	709	53	100	0.05	736	213	34	7	82	22
TK20113001G 7-3	inc in garnet	core	1.757276	0.122457	0.166619	0.004696	0.404	0.076492	0.004875	1030	46	993	26	1108	133	104	0.38	61	18	24	5	11	3
TK20113001G 7-4	inc in garnet	rim	0.937309	0.029901	0.095398	0.001923	0.632	0.071260	0.001762	671	16	587	11	965	51	114	0.04	723	84	28	3	68	8
TK20113001G 8-1	inc in garnet	rim	0.821724	0.045807	0.095651	0.003953	0.741	0.062307	0.002331	609	26	589	23	685	82	103	-	666	96	-	-	63	10
TK20113001G 8-2	inc in garnet	core	2.070687	0.091097	0.188508	0.007644	0.922	0.079668	0.001360	1139	31	1113	42	1189	34	102	0.26	1395	201	366	54	279	43
TK20113001G2 111-1	in garnet b.d.	mantle	1.539872	0.047903	0.147966	0.003120	0.678	0.075478	0.001726	946	19	890	18	1081	47	106	0.18	1204	124	221	16	188	18
TK20113001G2 111-2	in garnet b.d.	rim	0.784291	0.034890	0.097972	0.002183	0.501	0.058060	0.002236	588	20	603	13	532	87	98	0.04	699	72	30	2	68	7
TK20113001G2 111-3	in garnet b.d.	rim	0.747601	0.033970	0.094491	0.002114	0.492	0.057382	0.002270	567	20	582	12	506	89	97	0.09	692	71	63	4	66	6
TK20113001G2 112	inc in biotite	core	1.308895	0.059958	0.116030	0.002689	0.506	0.081815	0.003233	850	27	708	16	1241	79	120	0.16	406	42	64	5	50	5
TK20113001G2 113-1	in matrix	core	1.881409	0.054977	0.184617	0.003855	0.715	0.073911	0.001511	1075	20	1092	21	1039	42	98	0.33	1321	136	437	31	265	26
TK20113001G2 113-2	in matrix	core	1.853040	0.075884	0.183856	0.004104	0.545	0.073098	0.002510	1065	27	1088	22	1017	71	98	0.18	386	40	69	5	74	7
TK20113001G2 139-1	in garnet b.d.	rim	0.765100	0.029278	0.093823	0.002027	0.565	0.059144	0.001868	577	17	578	12	572	70	100	0.02	1110	114	23	2	103	10
TK20113001G2 139-2	in garnet b.d.	rim	0.974806	0.043874	0.095660	0.002181	0.507	0.073907	0.002868	691	23	589	13	1039	80	117	0.07	562	58	41	3	56	6
TK20113001G2 139-3	in garnet b.d.	mantle	1.157245	0.036667	0.112158	0.002370	0.667	0.074833	0.001767	781	17	685	14	1064	48	114	0.03	1478	152	47	3	172	17
TK20113001G2 14-1	inc in garnet	core	1.491455	0.061276	0.151684	0.005733	0.920	0.071313	0.001148	927	25	910	32	966	33	102	0.24	5099	416	1242	129	835	73
TK20113001G2 14-2	inc in garnet	rim	0.909514	0.046307	0.106493	0.004102	0.757	0.061942	0.002062	657	25	652	24	672	73	101	0.03	913	74	23	2	98	9
TK20113001G2 175-1	inc in sillimanite	core	1.490070	0.042759	0.153073	0.003183	0.725	0.070600	0.001396	926	18	918	18	946	41	101	0.09	1820	187	161	11	283	27
TK20113001G2 175-2	inc in sillimanite	mantle	0.769230	0.027397	0.093321	0.001992	0.599	0.059783	0.001704	579	16	575	12	596	63	101	0.04	1395	144	54	4	130	13
TK20113001G2 175-3	inc in sillimanite	rim	0.801347	0.041700	0.093132	0.002179	0.450	0.062405	0.002901	598	24	574	13	688	102	104	0.09	460	47	40	3	43	4
TK20113001G2 18-1	in garnet b.d.	core	1.207844	0.064420	0.132689	0.005225	0.738	0.066020	0.002375	804	30	803	30	807	77	100	0.13	625	60	79	3	87	8
TK20113001G2 18-2	in garnet b.d.	mantle	0.788112	0.040719	0.093454	0.003660	0.758	0.061163	0.002061	590	23	576	22	645	74	102	0.05	1136	109	56	2	108	10
TK20113001G2 18-3	in garnet b.d.	rim	0.794864	0.049268	0.093924	0.003764	0.646	0.061379	0.002903	594	28	579	22	653	105	103	0.04	484	46	22	1	46	4
TK20113001G2 182-1	inc in sillimanite	core	2.055492	0.057176	0.188102	0.003903	0.746	0.079254	0.001468	1134	19	1111	21	1178	37	102	1.11	1835	337	2029	347	432	86
TK20113001G2 184-1	inc in garnet overgrowing sillimanite	core	1.860032	0.072533	0.181679	0.004006	0.566	0.074253	0.002388	1067	26	1076	22	1048	66	99	0.40	506	93	201	34	103	20
TK20113001G2 184-2	inc in garnet overgrowing sillimanite	core	1.495085	0.069447	0.155541	0.003569	0.494	0.069714	0.002816	928	29	932	20	920	85	100	0.25	381	70	94	16	64	13
TK20113001G2 184-3	inc in garnet overgrowing sillimanite	rim	0.808067	0.046032	0.091987	0.002220	0.424	0.063712	0.003288	601	26	567	13	732	113	106	0.20	417	76	85	15	41	8
TK20113001G2 184-4	inc in garnet overgrowing sillimanite	mantle	1.294331	0.059205	0.098875	0.002320	0.513	0.094942	0.003728	843	27	608	14	1527	76	139	0.19	479	88	91	16	54	11
TK20113001G2 184-5	inc in garnet overgrowing sillimanite	core	1.675727	0.079980	0.167780	0.003899	0.487	0.072437	0.003020	999	31	1000	22	998	87	100	0.28	318	58	88	15	57	11
TK20113001G2 192-1	in garnet b.d.	core	1.651633	0.040849	0.156999	0.003206	0.826	0.076298	0.001064	990	16	940	18	1103	28	105	0.12	6366	1167	766	131	1050	209
TK20113001G2 192-2	in garnet b.d.	mantle	0.823632	0.029384	0.099030	0.002114	0.598	0.060321	0.001724	610	16	609	12	615	63	100	0.05	1475	270	68	12	147	29
TK20113001G2 192-3	in garnet b.d.	rim	0.791947	0.039698	0.091759	0.002121	0.461	0.062596	0.002784	592	23	566	13	695	98	105	0.10	581	107	60	10	55	11
TK20113001G2 194	inc in garnet	rim	0.967043	0.039974	0.089689	0.002005	0.541	0.078200	0.002719	687	21	554	12	1152	71	124	0.01	822	151	10	2	78	16
TK20113001G2 20-1	in garnet b.d.	core	1.524001	0.049630	0.157860	0.003344	0.650	0.070018	0.001732	940	20	945	19	929	52	99	0.12	1135	208	139	24	186	37
TK20113001G2 20-2	in garnet b.d.	rim	1.006391	0.048569	0.097808	0.002277	0.482	0.074626	0.003155	707	25	602	13	1058	88	118	0.06	515	95	32	6	54	11
TK20113001G2 20-3	in garnet b.d.	rim	0.759154	0.032658	0.095908	0.002117	0.513	0.057408	0.002120	574	19	590	12	507	83	97	0.07	899	165	66	11	87	17
TK20113001G2 22-1	inc in biotite	core	2.400719	0.138378	0.205153	0.008238	0.697	0.084872	0.003509	1243	42	1203	44	1313	82	103	0.75	226	22	168	7	56	5
TK20113001G2 22-2	inc in biotite	rim	0.816499	0.046978	0.092025	0.003654	0.690	0.064350	0.002679	606	27	568	22	753	90	107	0.05	639	61	33	1	60	6
TK20113001G2 25-1	inc in garnet	rim	0.939109	0.054403	0.092969	0.003709	0.689	0.073261	0.003077	672	29	573	22	1021	87	117	-	549	52	-	-	53	5
TK20113001G2 25-2	inc in garnet	mantle	0.883405	0.048286	0.102045	0.003965	0.711	0.062787	0.002414	643	26	626	23	701	84	103	0.01	678	55	4	0	70	6
TK20113001G2 26-1	inc in garnet	core	1.370360	0.066951	0.140976	0.005421	0.787	0.070500	0.002125	876	29	850	31	943	63	103	0.25	773	63	196	20	118	11
TK20113001G2 26-2	inc in garnet	rim	0.883020	0.053161	0.094975	0.003748	0.656	0.067431	0.003066	643	29	585	22	851	97	110	0.02	472	38	9	1	46	4
TK20113001G2 35-1	in garnet b.d.	rim	1.047205	0.061087	0.097704	0.003910	0.686	0.077736	0.003299	727	31	601	23	1140	87	121	0.10	482	46	47	2	51	5
TK20113001G2 35-2	in garnet b.d.	rim	0.757653	0.046495	0.092878	0.003712	0.651	0.059164	0.002755	573	27	573	22	573	105	100	0.08	525	50	41	2	49	5
TK20113001G2 49-1	in garnet b.d.	core	1.138704	0.044558	0.122445	0.003019	0.630	0.067448	0.002050	772	21	745	17	852	64	104	0.01	1021	43	7	0	125	5
TK20113001G2 49-2	in garnet b.d.	mantle	0.988029	0.053771	0.102564	0.002729	0.489	0.069867	0.003317	698	28	629	16	924	101	111	0.04	377	16	15	0	40	2
TK20113001G2 49-3	in garnet b.d.	rim	0.753095	0.049242	0.089904	0.003630	0.618	0.060753	0.003124	570	29	555	22	631	115	103	0.10	421	40	40	2	39	4
TK20113001G2 51-1	in matrix	rim	1.004553	0.062805	0.091972	0.003727	0.648	0.079216	0.003772	706	32	567	22	1178	97	124	0.09	384	37	36	2	38	4
TK20113001G2 51-2	in matrix	rim	0.809734	0.052226	0.092056	0.003717	0.626	0.063795	0.003209	602	30	568	22	735	110	106	0.13	413	39	55	2	39	4
TK20113001G2 51-3	in matrix	core	0.746170	0.040067	0.093768	0.003684	0.732	0.057714	0.002113	566	24	578	22	519	82	98	0.04	959	92	36	2	90	8
TK20113001G2 51-4	in matrix	core	0.777576	0.045226	0.095289	0.003781	0.682	0.059183	0.002517	584	26	587	22	574	95	100	0.01	634	61	4	0	61	6
TK20113001G2 78-1	in garnet b.d.	core	1.077080	0.041333	0.120362	0.002954	0.640	0.064902	0.001915	742	20	733	17	771	63	101	0.04	1177	49	45	1	142	5
TK20113001G2 78-2	in garnet b.d.	rim	0.857802	0.047275	0.095402	0.002531	0.481	0.065212	0.003150	629	26	587	15	781	105	107	0.14	415	17	57	1	41	2
TK20113001G2 84-1	inc in biotite	core	1.046815	0.042192	0.116211	0.002876	0.614	0.065332	0.002078	727	21	709	17	785	68	103	0.03	971	41	33	1	114	4
TK20113001G2 84-2	inc in biotite	mantle	0.810491	0.033538	0.099870	0.002472	0.598	0.058859	0.001952	603	19	614	15	562	74	98	0.06	1109	47	66	1	111	4
TK20113001G2 84-3	inc in biotite	rim	0.856733	0.035323	0.103375	0.002560	0.601	0.060107	0.001981	628	20	634	15	607	73	99	0.06	1068	45	60	1	111	4
TK20113001G2 87-1	in matrix	core	2.074733	0.081129	0.194254	0.004820	0.634	0.077462	0.002341	1140	27	1144	26	1133	61	100	0.24	575	24	141	3	119	5
TK20113001G2 87-2	in matrix	core	1.942353	0.068773	0.192290	0.004679	0.687	0.073260	0.001884	1096	24	1134	25	1021	53	97	0.28	1037	44	292	6	212	8
TK20113001G2 87-3	in matrix	rim	0.783073	0.043728	0.092498	0.002449	0.474	0.061400	0.003019	587	25	570	14	653	109	103	0.11	435	18	47	1	41	2
TK20113001G2 87-4	in matrix	rim	0.831999	0.046327	0.098648	0.002610	0.475	0.061169	0.002997	615	26	606	15	645	109	101	0.02	413	17	6	0	40	2
TK20113001G2 92-1	in garnet b.d.	rim	0.725471	0.043265	0.092910	0.002247	0.405	0.056631	0.003087	554	26	573	13	477	125	97	0.10	362	37	35	3	34	3
TK20113001G2 92-2	in garnet b.d.	core	1.910877	0.102343	0.190619	0.005093	0.499	0.072705	0.003375	1085	36	1125	28	1006	97	96	0.41	206	9	85	2	43	2
TK20113001G2 92-3	in garnet b.d.	mantle	0.834318	0.035060	0.102007	0.002533	0.591	0.059320	0.002011	616	20	626	15	579	75	98	0.01	1015	43	14	0	103	4

Table 2 Kawakami et al.